Supplementary Information

Electrosynthesis of Jahn–Teller Distorted Co^{IV}=O Species for Efficient Oxidant-Free Water Purification and Resource Recovery

Bing Zhou[1, #], Furong Guo[1, #], Long Zhao[1], Huan Yang[2], Lufa Hu[1], Yang Wu[3], Yibing Ma[3], Yancai Yao[1, *], Lizhi Zhang[1]

[1]State Key Laboratory of Green Papermaking and Resource Recycling, School of Environmental Science and Engineering, Shanghai Jiao Tong University, Shanghai 200240, China.

[2]Zhejiang Materials Industry Guanghua Civil Explosive Materials CO., Ltd. Quzhou, Zhejiang 324400, China

[3]National Observation and Research Station of Coastal Ecological Environments in Macao, Macau Environmental Research Institute, Macau University of Science and Technology, Macao SAR 999078, China

[#]These authors contributed equally: Bing Zhou, Furong Guo

*Correspondence and requests for materials should be addressed to Yancai Yao (yyancai@sjtu.edu.cn).

10 texts, 69 figures, 9 tables

Text S1: Characterizations

X-ray powder diffraction (XRD) patterns were collected on a Shimadzu XRD-6100 diffractometer using Cu Kα radiation (λ = 0.15418 nm). Aberration-corrected high-angle annular dark-field scanning transmission electron microscopy (AC HAADF-STEM) images were acquired using a Thermo Scientific Spectra 300 microscope operated at 300 kV. Transmission electron microscopy (TEM) images were obtained on a Titan^{TM} G2 60-300 electron microscope. Metal content was quantified by inductively coupled plasma optical emission spectrometry (ICP-OES) using a Thermo Scientific iCAP PRO instrument. X-ray photoelectron spectroscopy (XPS) measurements were carried out on a Thermo Scientific K-Alpha spectrometer equipped with a monochromatic Al Kα X-ray source (hν = 1486.6 eV). All XPS spectra were energy-calibrated by setting the adventitious hydrocarbon C 1s peak to 284.8 eV. Raman spectra were recorded on a Renishaw inVia Qontor confocal Raman microscope with a 532 nm laser excitation source. *In situ* attenuated total reflectance Fourier transform infrared (ATR-FTIR) spectroscopy was performed on a Nicolet iS50 spectrometer (Thermo Fisher Scientific) coupled with a spectro-electrochemical cell supplied by Linglu Instrument (Shanghai) Co., Ltd. X-ray absorption fine structure (XAFS) data were collected at the Singapore Synchrotron Light Source (SSLS). Energy calibration was performed using a standard cobalt foil as reference. The extended X-ray absorption fine structure (EXAFS) data were processed using the ATHENA module of the IFEFFIT software package.

Text S2: *In situ* Raman measurements

In situ Raman measurements were performed using a customized cell with a saturated Ag/AgCl reference electrode and a Pt wire counter electrode in 50 mmol/L K_2SO_4. An In-via microspore with a water-immersion objective (Olympus, 50X) was used to focus and collect the incident and scattered laser light during electrochemical measurements. The Raman signals were recorded *in situ* under different applied potentials spanning from +1.5 to 2.1 V vs. RHE.

Text S3: *In situ* ATR-FTIR measurements

In situ attenuated total reflection-Fourier transform infrared (ATR-FTIR) measurements were conducted using a Nicolet-6700 spectrometer (Thermo Scientific). A custom three-electrode cell with a zinc selenide (ZnSe) window was applied in the test. The working electrode was a catalyst-coated glassy carbon electrode against the ZnSe window. A saturated Ag/AgCl reference electrode and a

platinum wire were employed as the reference and counter electrodes, respectively. All measurements were carried out in a 50 mM K_2SO_4 electrolyte. We collected ATR-FTIR spectra continuously at potentials from +1.5 to +2.2 V vs. RHE, using a resolution of 4 cm^{-1} and a 30 s interval between scans.

Text S4: Quantification of •OH

Benzoic acid (BA) was used as a probe to quantify •OH. It reacts with •OH to form three hydroxylated products: ortho-, meta-, and para-hydroxybenzoic acid (o-HBA, m-HBA, and p-HBA), with a yield ratio of 1.7 : 2.3 : 1.2, respectively. The concentration of p-HBA, which was readily quantified by high-performance liquid chromatography (HPLC), was used to calculate the total •OH concentration according to Equation (1). The HPLC analysis was performed using an Agilent SB-C18 column with a mobile phase of 0.1% acetic acid and acetonitrile (70:30, v/v) at a flow rate of 1.0 mL/min. The column temperature and detection wavelength were set at 30 °C and 270 nm, respectively.

$$\text{Cumulative}[\bullet OH] = [\text{p-HBA}] \times 5.87 \quad (1)$$

Text S5: Quantification of H_2O_2

The concentration of H_2O_2 was determined spectrophotometrically by measuring the formation of I_3^-. This method involved the preparation of two solutions: Solution A was prepared by dissolving 33 g of KI, 1.4 g of KOH, and 0.1 g of $(NH_4)_6Mo_7O_{24}.4H_2O$ in 500 mL of distilled water, and was stored in the dark to prevent the oxidation of I^-. Solution B was an aqueous solution of potassium hydrogen phthalate (10 g in 500 mL of distilled water). Prior to analysis, the pH of the sample was adjusted to 7.0. Then, the sample was mixed with equal volumes of Solution A and Solution B. After a reaction time of 5 minutes, the UV-Vis absorption spectrum of the mixture, which contained I_3^-, was recorded at 352 nm.

Text S6: Phytotoxicity assays using Pisum sativum (pea) sprouts

Prior to the experiments, both the raw electroplating wastewater and the treated wastewater were adjusted to a neutral pH using diluted HCl and subsequently filtered to remove suspended solids. Pisum sativum (pea) seeds were washed and soaked in deionized water overnight. The seeds were then cultivated on cotton beds saturated with the respective wastewater samples. Their growth was subsequently tracked and documented at predetermined time points.

Text S7: Energy consumption calculations

The electric energy per order (EEO, kWh m^{-3}) represents the amount of electric energy required for a one-log order of magnitude reduction in the target contaminant concentration within a unit volume. This is expressed by the following equation:

$$EEO = \frac{UIt}{V \log \frac{C_0}{C_t}}$$

Where U and I are the applied voltage (V) and current (A) of the electrochemical cell, respectively, V (L) is the volume of the treated wastewater, C_0 and C_t are the target contaminant concentrations at time = 0 h and time = t h, respectively.

Text S8: Techno-economic analysis (TEA)

Technoeconomic analysis of EOCR process

We performed a preliminary TEA to evaluate and compare the financial implications of the conventional multi-stage physicochemical treatment (MSPT) and electrochemical oxidation-coupled reduction (EOCR) process. A modified TEA model proposed by Sargent and Huang et al [1, 2] was adopted in this work.

The specific assumptions for the TEA are as follows:

1. The anticipated service life of the electrolyzer is 10 years, and the working time per year is 350 days.

2. The electricity price is considered to be 0.07 \$ kWh^{-1}.

3. The operating voltage is set as 3.9 V based on the experiements.

4. The cost of the balance of plants is set as 58% of the cost of the electrolyzer.

5. The cost of separation equipment is assumed to be 20% of the electrolyzer cost.

6. The maintenance cost is set as 2.5% of the electrolyzer cost.

7. The separation cost is assumed to be 30% of the electricity cost.

Based on the laboratory experiments with a flow rate of 2 L/h, wastewater containing 17.8 mg/L Ni and 44.2 mg/L Zn, anode electrode total area of 1620 cm^2 (with a immeresed area of 1300 cm^2) a current density of 3.0 mA/cm^2 (30 A/m^2), and an electrolytic cell volume of 5.6 L, a scale-up calculation was performed for the industrial design. The projected full-scale plant is designed to treat 1000 m^3 of wastewater per day, operating for 350 days per year, resulting in an annual treatment capacity of 3.50×10^5 m^3.

The Ti mesh and carbon felt electrodes constitute the dominant portion of the total electrode cost. Their prices are 480 ¥ m^{-2} and 200 ¥ m^{-2}, respectively (sources: Taobao links, https://e.tb.cn/h.7fRKkNNXu9z5vGc?tk=qIIQfCSaSHL, https://e.tb.cn/h.74K9KJFwXGNVo6g?tk=ZNVhfCSB2Qj). The chemicals, material and energy cost for fabricating the P-Co_1O_5 anode is provided in Table S7.

Cost of P-Co_1O_5 anode = 77.56 \$ m^{-2} (exchange rate: 1 USD = 7.1 ¥)

Total electrode cost = anode + cathode = 77.56 \$ m^{-2} + 200 ¥ m^{-2} /7.1 ¥ $\$^{-1}$ = 105.73 \$ m^{-2}

The required total electrode area for the industrial system was estimated by scaling up from the experimental conditions. Using the laboratory flow rate (2 L/h) and electrode area (1300 cm^2) as the basis, the calculation is as follows:

Required electrode area = $\frac{1000\ m^3}{2*24\ 10^{-3} m^{-3}}$ × 1300 cm^2 × $\frac{1\ m^2}{10^4\ cm^2}$ = 2708.3 m^2

The required total current is calculated as:

Total current： = $\frac{30\ A}{m^2}$ × 2708.3 m^2 = 81250 A

The input power was calculated as:

Power = 81250 A × 3.9 V = 316875 W ≈ 316.9 kW

The reference electrolyzer cost was \$ 460 kW^{-1}. Based on the reference operating conditions, the electrolyzer cost per area was calculated as follows:

Electrolyzer cost per area = \$ 460 kW^{-1} × $\frac{0.003\ A}{cm^2}$ × 3.90 V × $\frac{10^4\ cm^2}{m^2}$ × $\frac{kW}{1000}$ = 53.82 \$ m^{-2}

Capital cost:

1. Electrolyzer: = 2708.3 m^2 × 53.82 \$ m^{-2} = 145761 \$
2. Balance of plant: = 145761 \$ × 58%= 84846 \$
3. Separation equipment: 145761 \$ × 20% = 29152 \$

Operation cost:

4. Electricity: = 316.9 kW/h × 24 h/day × 350 day/year × 0.07 \$/kW = 186519 \$/year
5. Maintenance: = 145761 \$ × 2.5% = 3644 \$
6. Separation: 186519 \$ × 30% = 55956 \$
7. Material cost: 105.73 \$/ m^2 × 2708.3 m^2 = 286349 \$

The total cost: 145761 \$ + 84846 \$ + 29152 \$+ 186519 \$ + 3644 \$ + 55956 \$+ 286349 \$ = 792227 \$

Unit wastewater treatment cost: $\frac{792227\ \$}{350\ day*1000\ m^3\ day^{-1}}$ = 2.26 \$ m^{-3}

Text S9: Life cycle assessment analysis (LCA)

The assessment was carried out in accordance with the guidelines established by ISO 14040. Life cycle inventory data were sourced from the Ecoinvent database, version 3.9.

Based on the active material calculation of the electrochemical pilot-scale EOCR device for LCA:

The wastewater contains approximately 62 mg/L heavy metal including 17.8 mg/L Ni and 44.2 mg/L Zn.

As a result, the total treatment amount of 1 kg heavy metal = 1 kg /(62 mg/L) = 16129 L = 16.13 m^3

Text S10: DFT calculation details

The Vienna Ab Initio Package (VASP) was employed to perform all the density functional theory (DFT) calculations within the generalized gradient approximation (GGA) using the Perdew, Burke, and Enzerhof (PBE) formulation [3, 4]. The projected augmented wave (PAW) potentials were applied to describe the ionic cores and take valence electrons into account using a plane wave basis set with a kinetic energy cutoff of 500 eV. The energy criterion is set to 10^{-5} eV in iterative solution of the Kohn-Sham equation. The Brillouin zone integration is performed using a 3×3×1 k-mesh. All the structures are relaxed until the residual forces on the atoms have declined to less than -0.02 eV/Å.

DFT+U calculations were performed with Ueff values of 3.9 eV and 4.5 eV for Ti 3d and Co 3d to correct the strong electron-correlation[5]. Thermal and zero-point energy (ZPE) corrections were calculated over Γ points. The Gaussian smearing method with an electronic temperature of kBT = 0.05 eV was employed. The Gibbs free energy change (ΔG) of the elementary step was estimated using:

$$\Delta G = \Delta EDFT + \Delta EZPE - T\Delta S$$

where ΔEDFT is the change in the electronic energy difference calculated by DFT, ΔEZPE is the change in the zero–point energy, T is the temperature (298.15 K) and ΔS is the entropy change. The ZPE and ΔS of the water oxidation intermediate species were computed from the vibrational frequencies over G points, in which only the adsorbate vibrational modes were calculated explicitly, while the electrocatalyst was fixed.

The model of amorphous structure was constructed by the ab-initio molecular dynamics (AIMD) simulations[6, 7]. A fixed volume NVT ensemble was used to conduct anneal-to-quench process from 1500 K to 300 K with a series of AIMD simulations, and each experiment was conducted at a constant temperature. Initial temperature of 1500 K was chosen to melt the P-Co_1O_5/TiO_x system, and 3 ps with a time step of 1 fs was given to optimize the configuration. The structure obtained from previous AIMD simulation at 1500 K was used as the input structure for the next lower temperature (300 K), where the AIMD simulation was run for 10 ps to fully reach its equilibrium configuration. A gamma-point only k-mesh was used to sample Brillouin zone for calculations performed on amorphous structures.

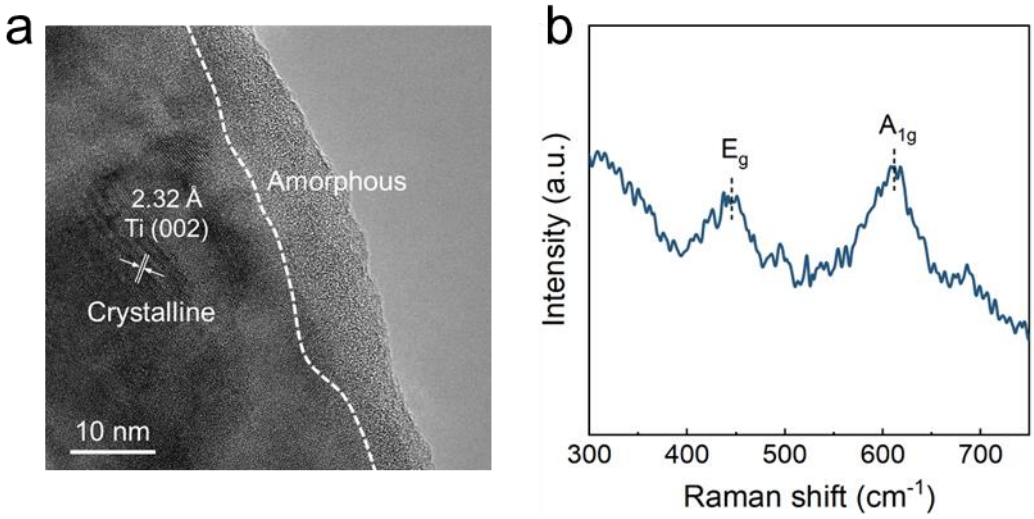

Supplementary Figure S1. (a) High-resolution TEM image and (b) Raman spectra of Ti mesh.

The combination of a distinct amorphous layer observed on the surface of metallic Ti by HRTEM and the characteristic Raman peaks of rutile (E_g and A_{1g} modes at 465 and 625 cm^{-1})[8] indicated that the amorphous substance was a titanium oxide (TiO_x).

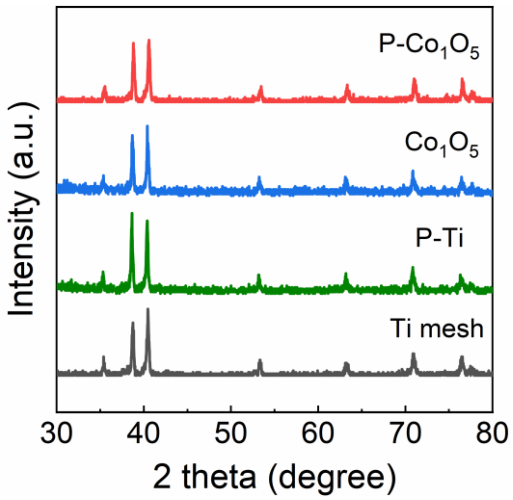

Supplementary Figure S2. XRD patterns of Ti mesh, P-Ti, Co_1O_5 and P-Co_1O_5.

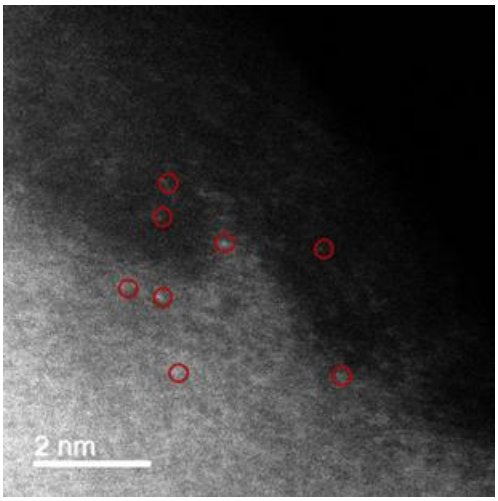

Supplementary Figure S3. AC-HADDF-STEM image of Co_1O_5.

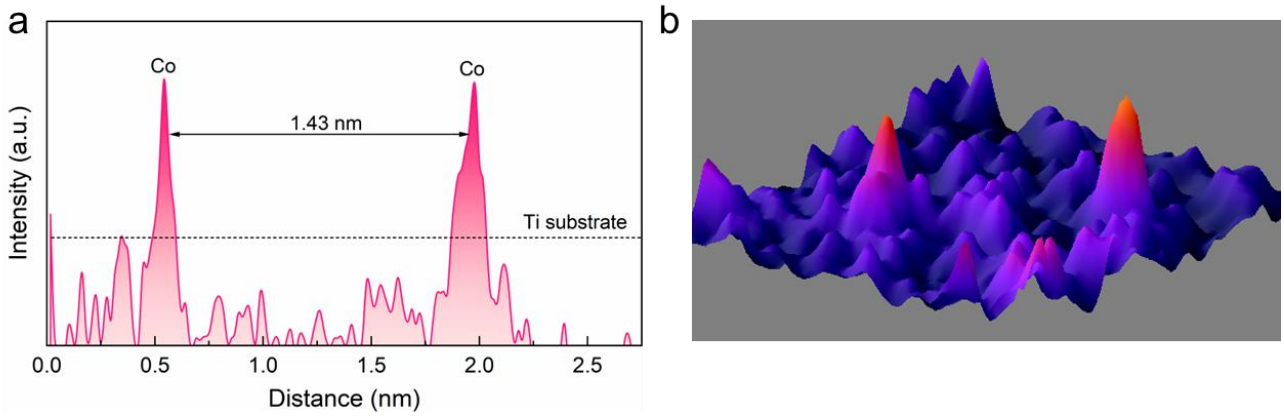

Supplementary Figure S4. The line intensity profile and 3D intensity profile of P-Co_1O_5.

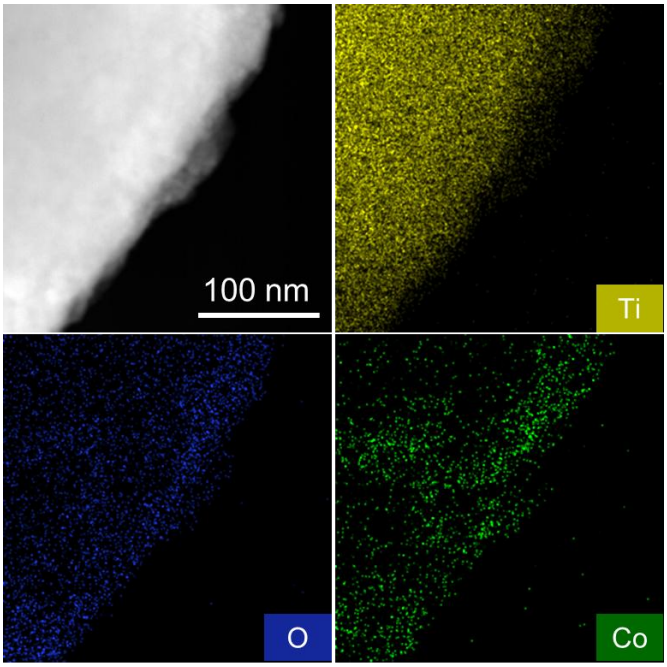

Supplementary Figure S5. EDX elemental mappings of Co_1O_5.

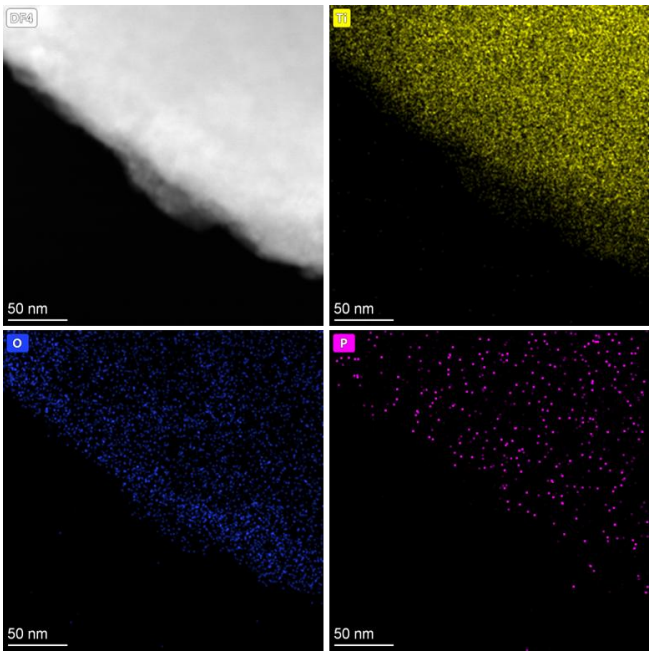

Supplementary Figure S6. EDX elemental mappings of P-Ti.

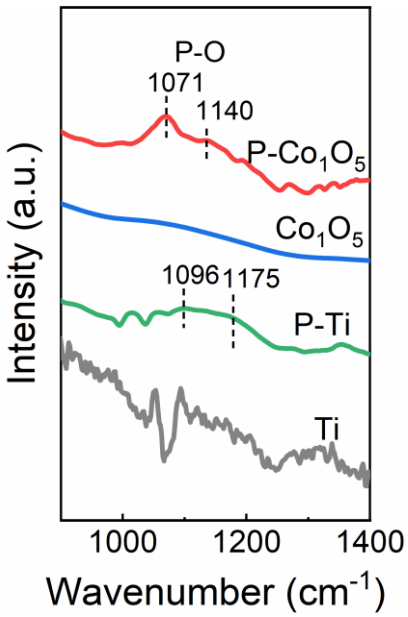

Supplementary Figure S7. Fourier transform infrared spectroscopy (FTIR) spectra of Ti, P-Ti, Co_1O_5 and P-Co_1O_5.

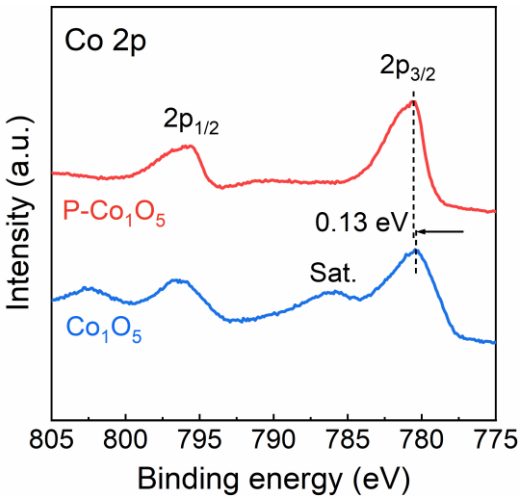

Supplementary Figure S8. High-resolution Co 2p XPS spectra of Co_1O_5 and P-Co_1O_5.

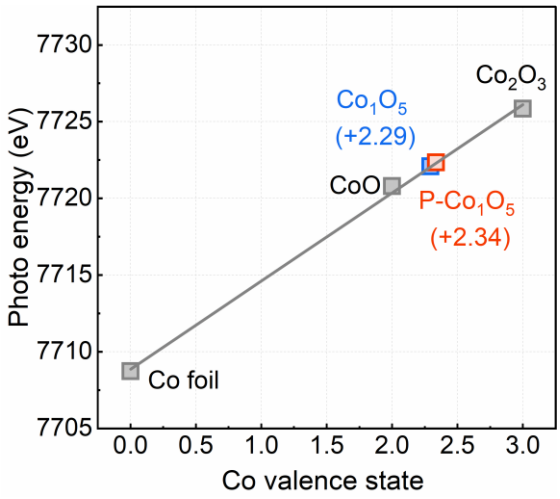

Supplementary Figure S9. Co oxidation state in Co_1O_5 and P-Co_1O_5 obtained from the Co K-edge XANES spectra.

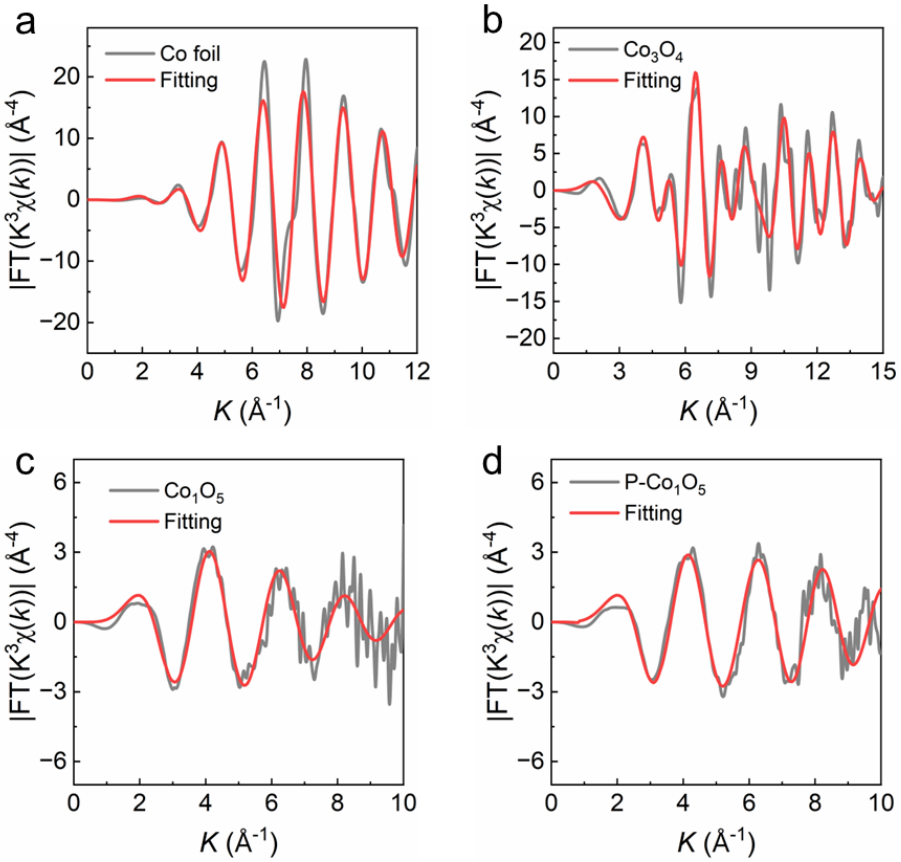

Supplementary Figure S10. The k-space fitting curves at Co K-edge of (a) Co foil and (b) Co_3O_4, (c) Co_1O_5 and (d) P-Co_1O_5. The fitting structural parameters were displayed in Supplementary Table S1.

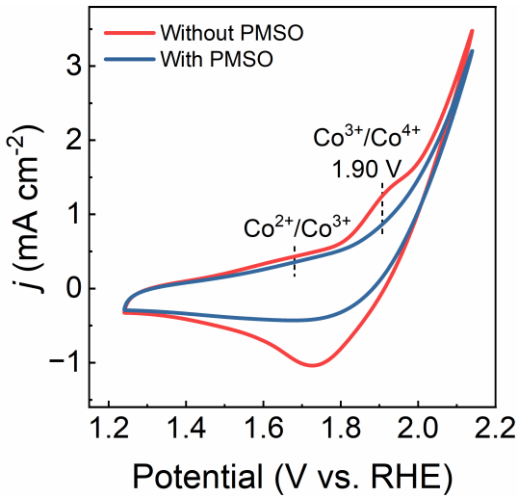

Supplementary Figure S11. CV curves of P-Co_1O_5 before and after the addition of PMSO.

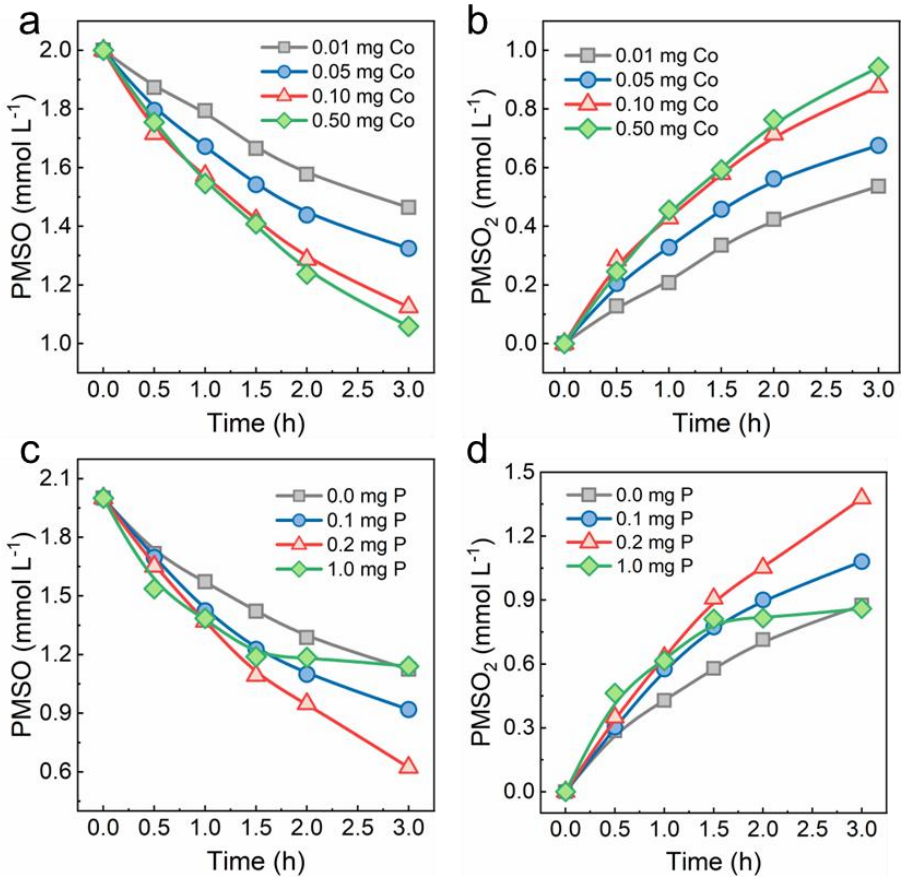

Supplementary Figure S12. Optimization of electrode performance. The effect of Co dosage (a, b) of Co_1O_5 and P precursor dosage (c, d) in P-Co_1O_5 on the conversion of PMSO into $PMSO_2$. The optimized dosage of Co and P were 0.1 and 0.2 mg, respectively.

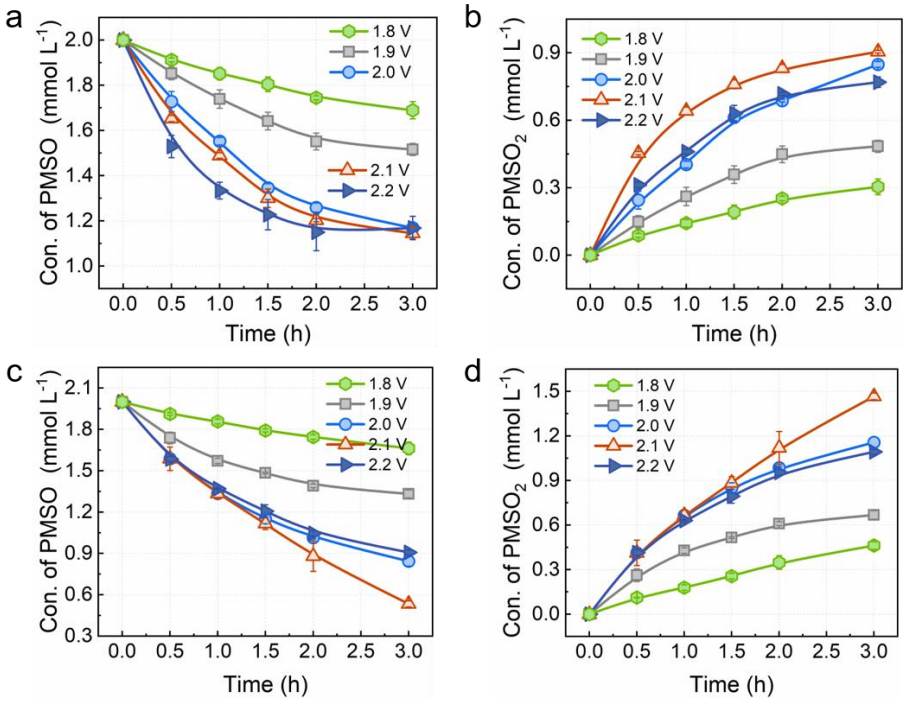

Supplementary Figure S13. The concentration of (a) PMSO and (b) $PMSO_2$ measured at the applied potentials from 1.8 V to 2.2 V vs. RHE using a Co_1O_5 anode. (c, d) Corresponding concentrations obtained with a P-Co_1O_5 anode.

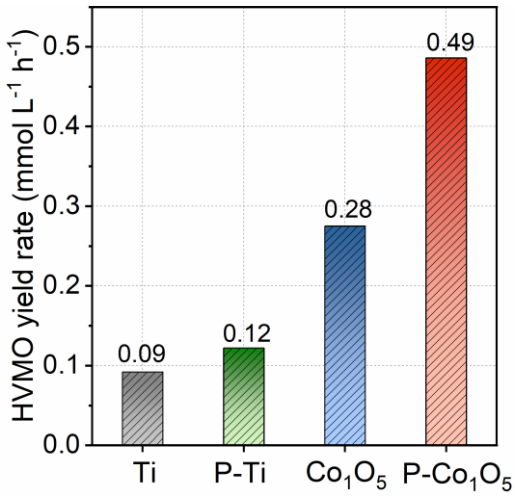

Supplementary Figure S14. The HVMO yield of Ti mesh, P-Ti, Co_1O_5 and P-Co_1O_5.

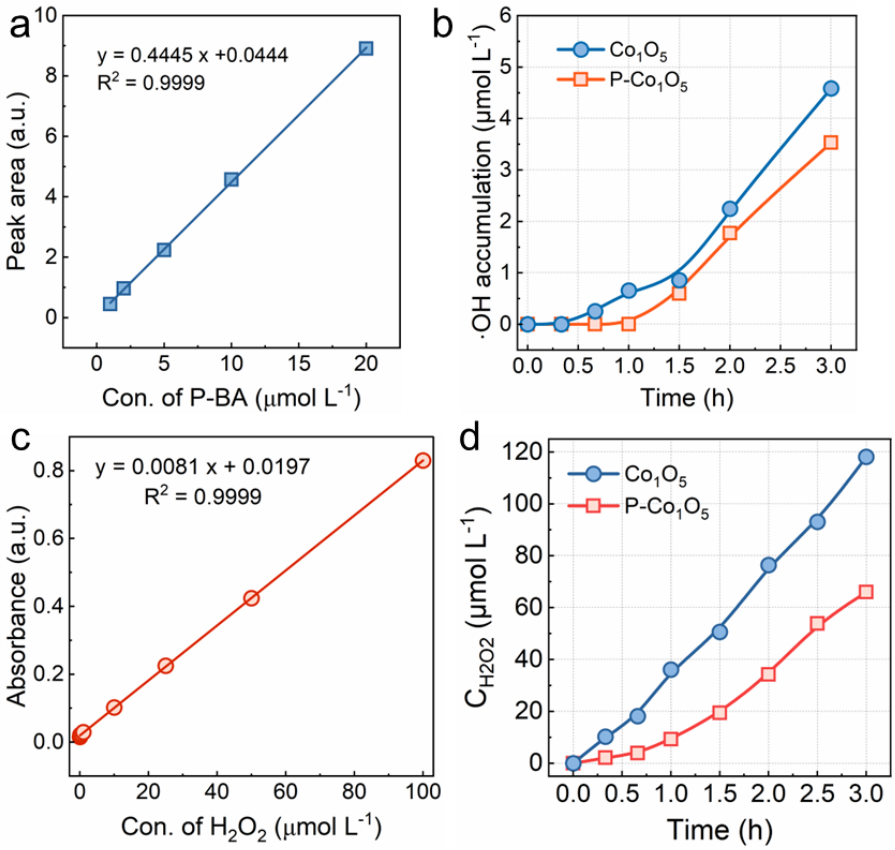

Supplementary Figure S15. (a) Standard curve for quantifying ·OH using P-BA and (b) the corresponding ·OH concentrations generated by Co_1O_5 and P-Co_1O_5 anodes. (c) Standard curve for H_2O_2 quantification and (d) H_2O_2 concentrations produced by the two anodes at 2.1 V vs. RHE.

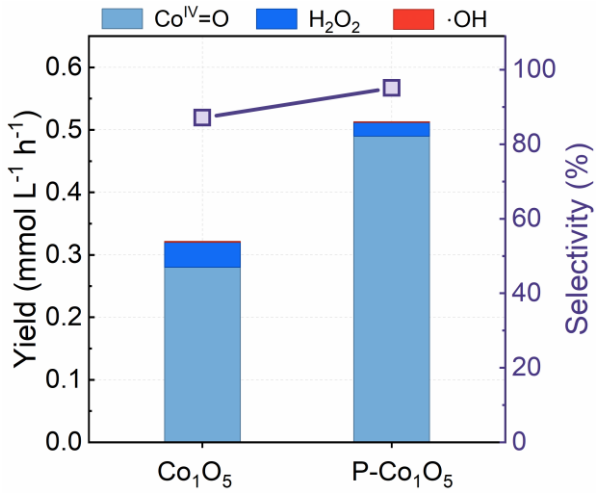

Supplementary Figure S16. Active species selectivity of Co_1O_5 and P-Co_1O_5 in H-type cell at 2.1 V vs. RHE.

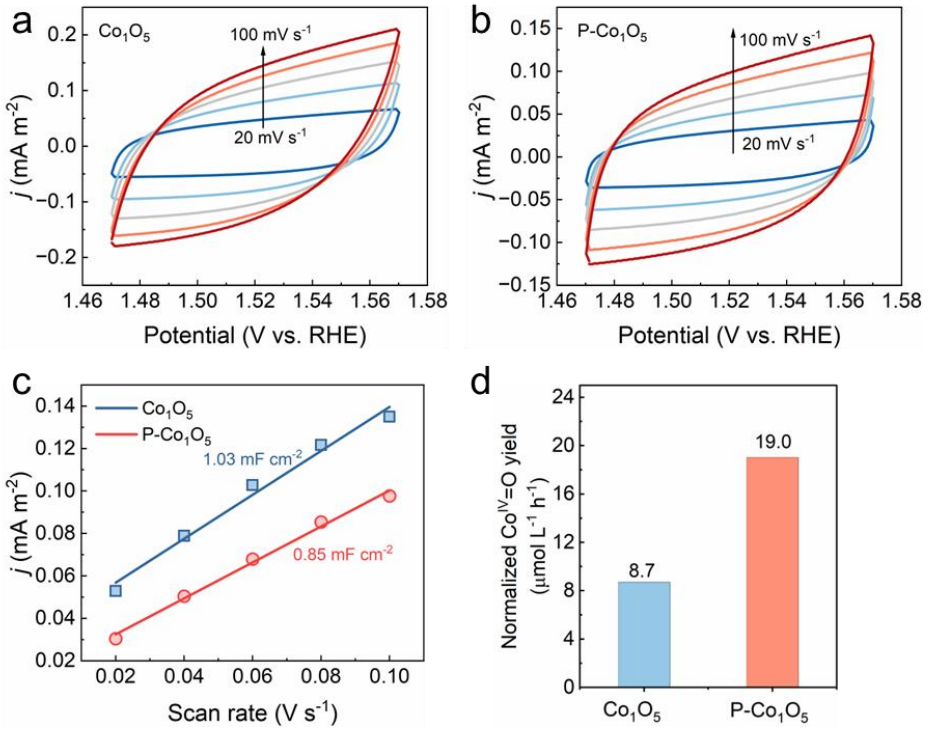

Supplementary Figure S17. CV curves of (a) Co_1O_5 and (b) P-Co_1O_5 with different scan rates from 20 to 100 mV s^{-1} (c) Plots of the current density versus the scan rates for Co_1O_5 and P-Co_1O_5. (d) ECSA-normalized Co^{IV}=O yield rate of Co_1O_5 and P-Co_1O_5 at 2.1 V versus RHE. The specific capacitance was obtained by plotting a function between currents density and scan rate. The calculated specific capacitance was 1.03 mF cm^{-2} for Co_1O_5 and 0.85 mF cm^{-2} for P-Co_1O_5. Generally, the specific capacitance for a flat surface is adopted to be 40 μF cm^{-2}.

$$A_{ECSA}^{Co1o5} = \frac{1030\ \mu F\ cm^{-2}}{40\ \mu F\ cm^{-2}} = 25.75_{\ ECSA} \quad (8)$$

$$A_{ECSA}^{P-Co1O5} = \frac{850\ \mu F\ cm^{-2}}{40\ \mu F\ cm^{-2}} = 21.25_{\ ECSA} \quad (9)$$

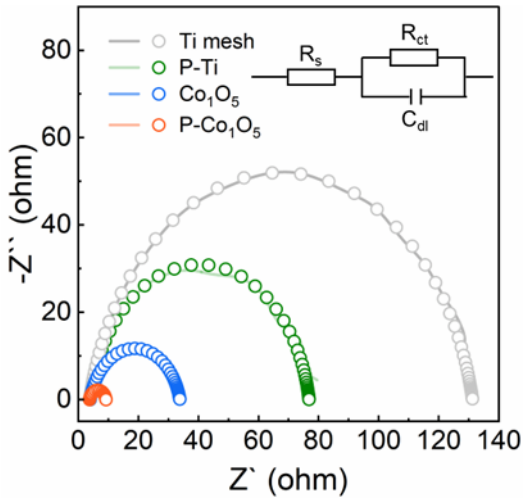

Supplementary Figure S18. EIS curves of Ti mesh, P-Ti, Co_1O_5 and P-Co_1O_5. (Potential: 2.1 V vs. RHE; 50 mM K_2SO_4; frequence range: 100000~0.1 Hz; amplitude: 5 mV).

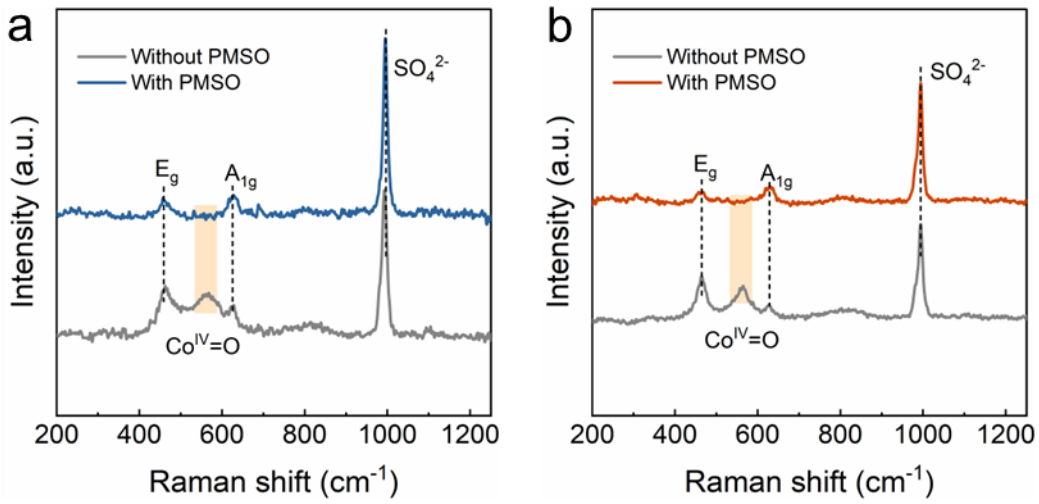

Supplementary Figure S19. *In situ* electrochemical Raman spectra of (a) Co_1O_5 and (b) P-Co_1O_5 before and after the addition of PMSO.

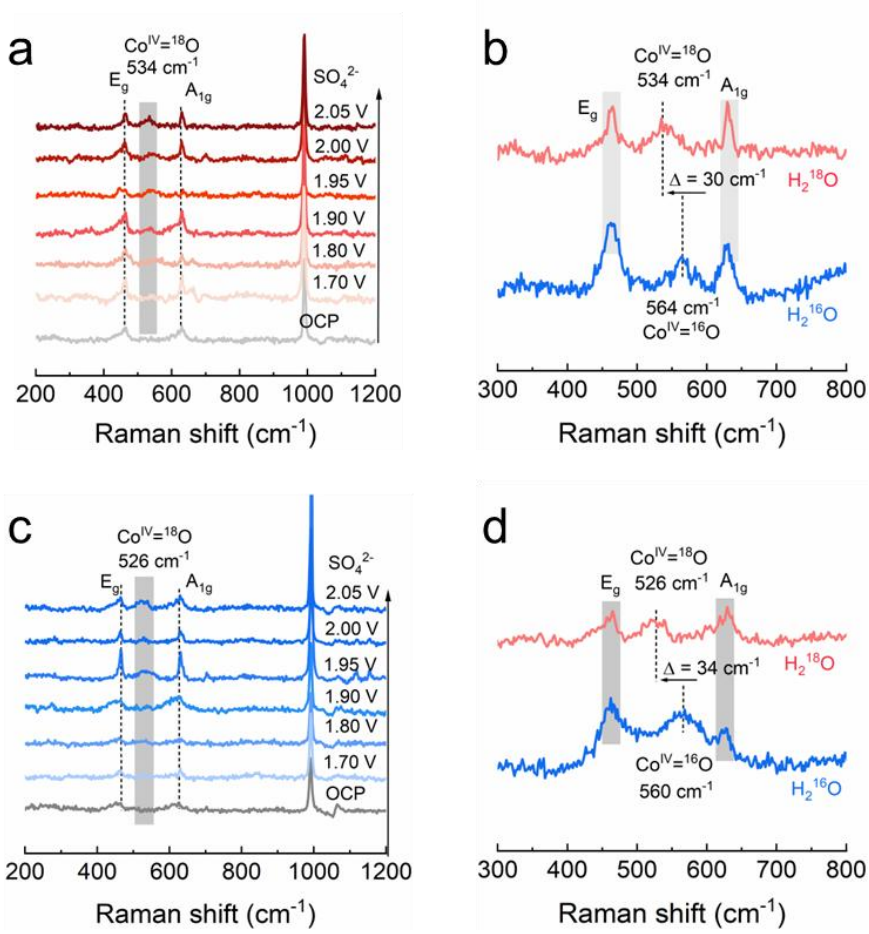

Supplementary Figure S20. *In situ* electrochemical Raman spectra of P-Co_1O_5 recorded in (a) $H_2{}^{18}O$, (b) the comparative spectra in $H_2{}^{18}O$ and $H_2{}^{16}O$. *In situ* electrochemical Raman spectra of Co_1O_5 recorded in (c) $H_2{}^{18}O$ and (d) the comparative spectra in $H_2{}^{18}O$ and $H_2{}^{16}O$.

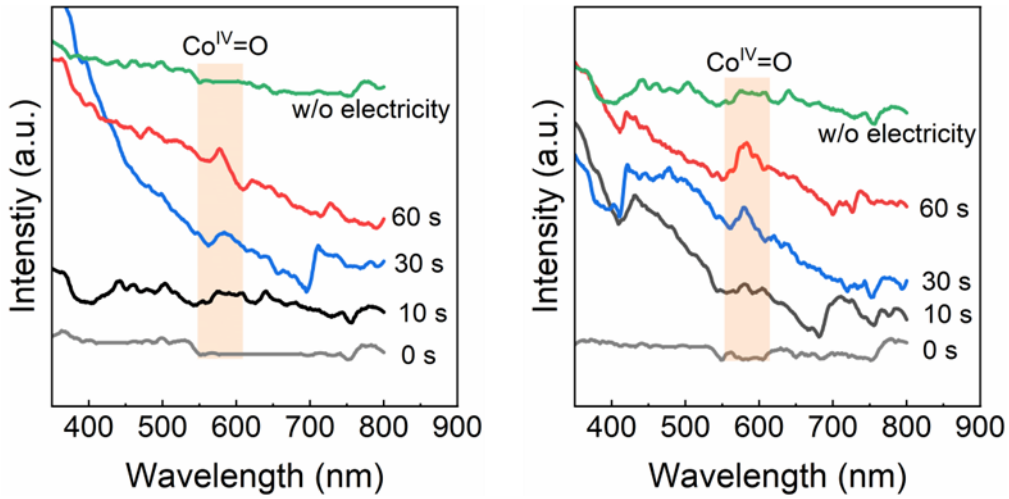

Supplementary Figure S21. Time-dependent *in-situ* electrochemical UV-Vis absorption spectra of (a) Co_1O_5 and (b) P-Co_1O_5 at 2.1 V.

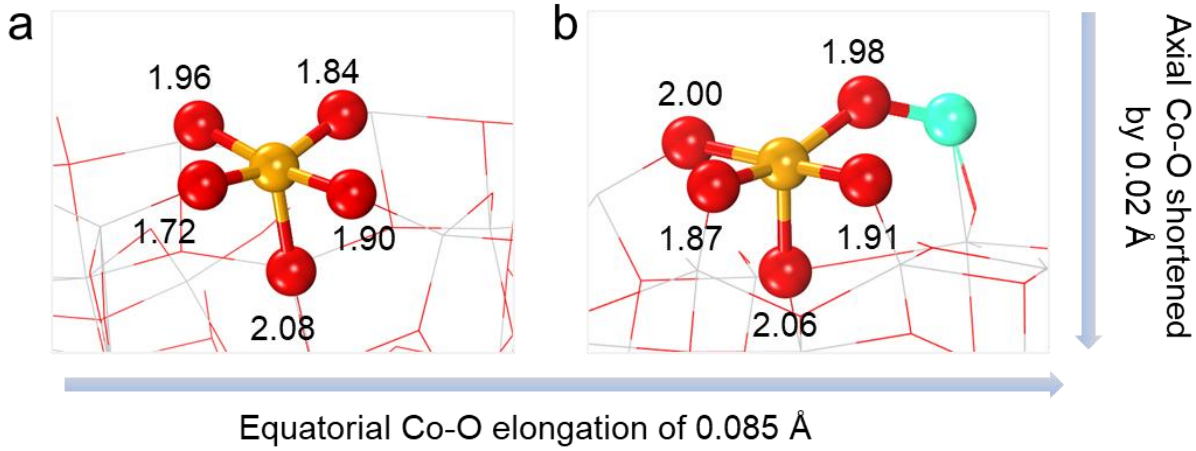

Supplementary Figure S18. Optimized structure models and bond length analysis of Co_1O_5 and P-Co_1O_5. The cyan, silver, red and cyan atoms represent Co, Ti, O and P atoms, respectively.

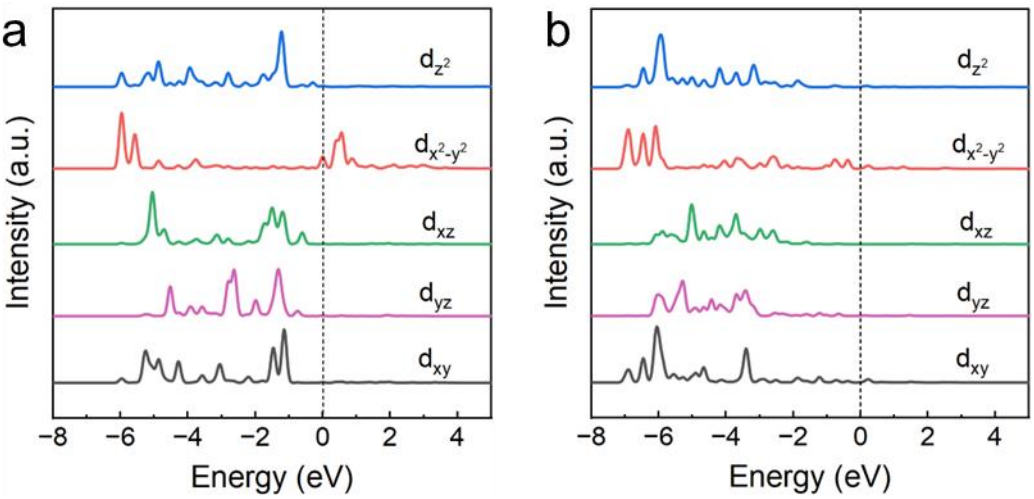

Supplementary Figure S19. Detailed the projected d-orbital density states of (PDOS) of Co in (a) Co_1O_5 and (b) P-Co_1O_5.

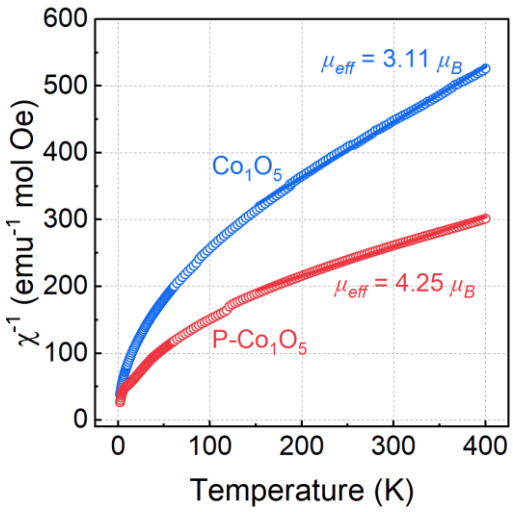

Supplementary Figure S24. 1/χ (where χ is susceptibility) versus T curves with Curie-Weiss fitting of Co_1O_5 and P-Co_1O_5.

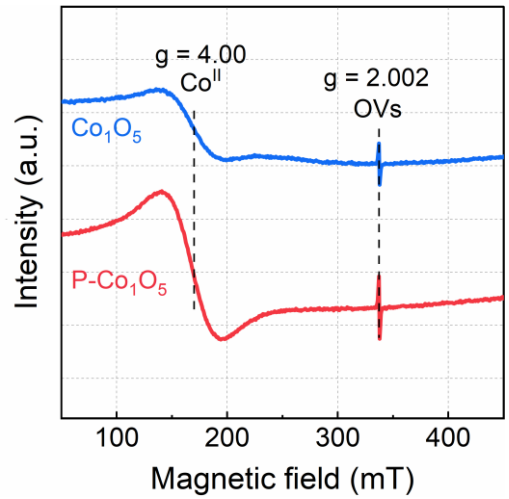

Supplementary Figure S25. Continuous-wave (CW) X-band EPR spectrum of Co_1O_5 and P-Co_1O_5.

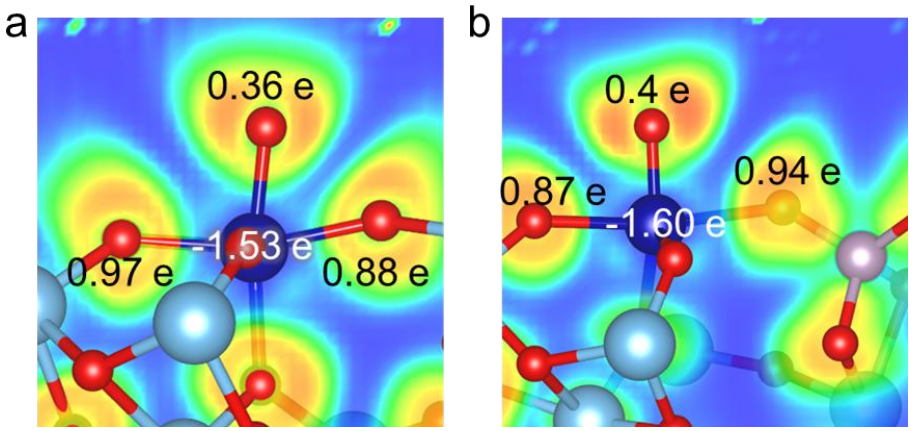

Supplementary Figure S26. Electron localization function (ELF) analysis of Co^{IV}=O in Co_1O_5 and (b) P-Co_1O_5.

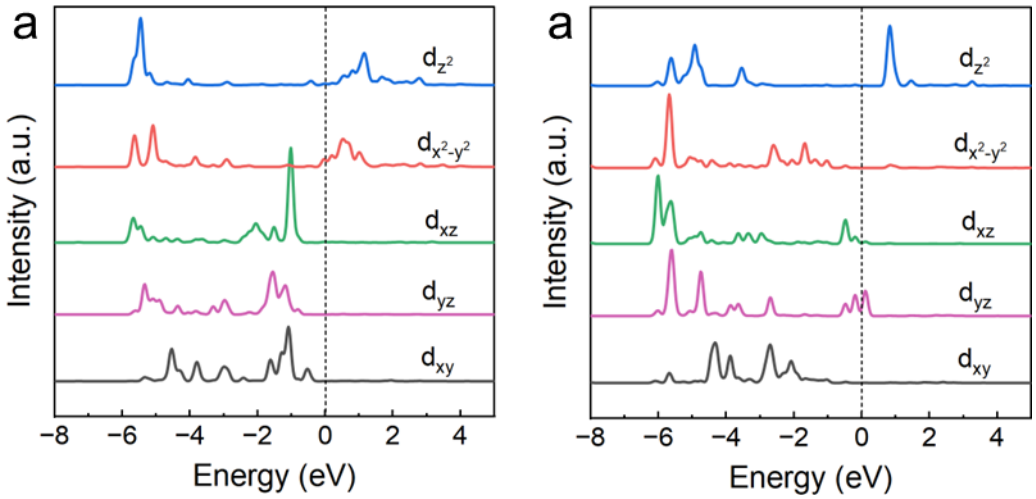

Supplementary Figure S27. Detailed the projected d-orbital density states of (PDOS) of Co atoms after formation of Co^{IV}=O in (a) Co_1O_5 and (b) P-Co_1O_5.

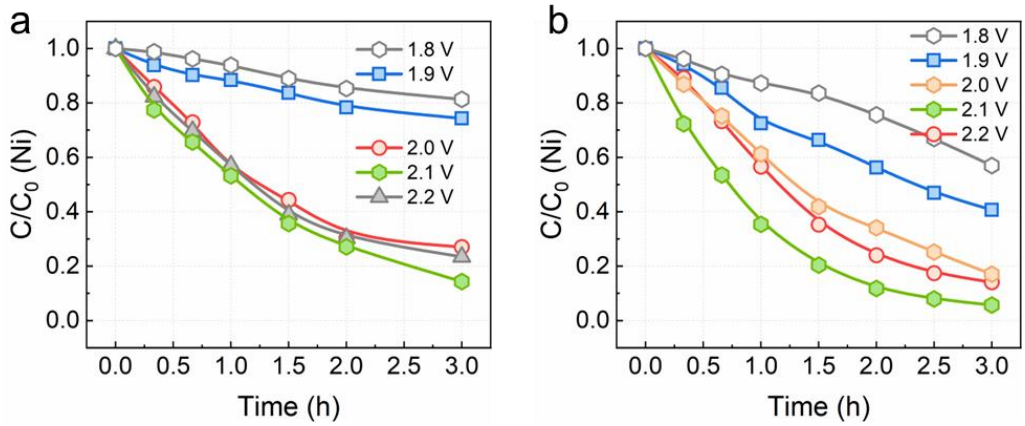

Supplementary Figure S28. Time-dependent total Ni concentration during the Ni-EDTA decomplexation with (a) Co_1O_5 and (b) P-Co_1O_5.

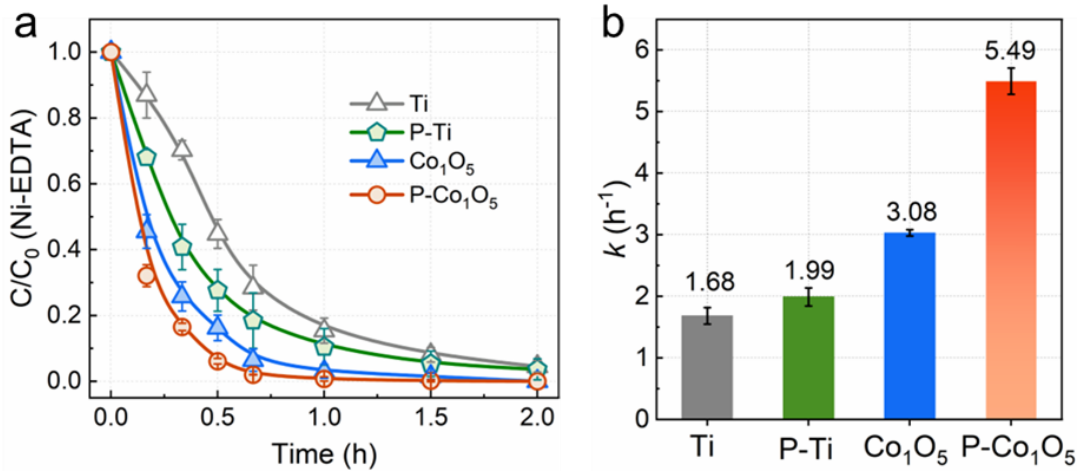

Supplementary Figure S29. (a) Ni-EDTA decomplexation efficiency of Ti mesh, P-Ti, Co_1O_5 and P-Co_1O_5. (b) Corresponding observed rate constant.

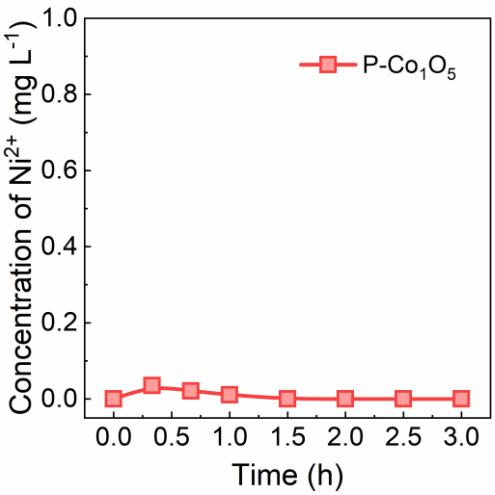

Supplementary Figure S30. Concentration of free Ni^{2+} during Ni-EDTA decomplexation. The concentration was calculated via the difference in total Ni (measured by ICP-OES) before and after pH adjustment to 12 and filtration via 0.22 μm filter membrane.

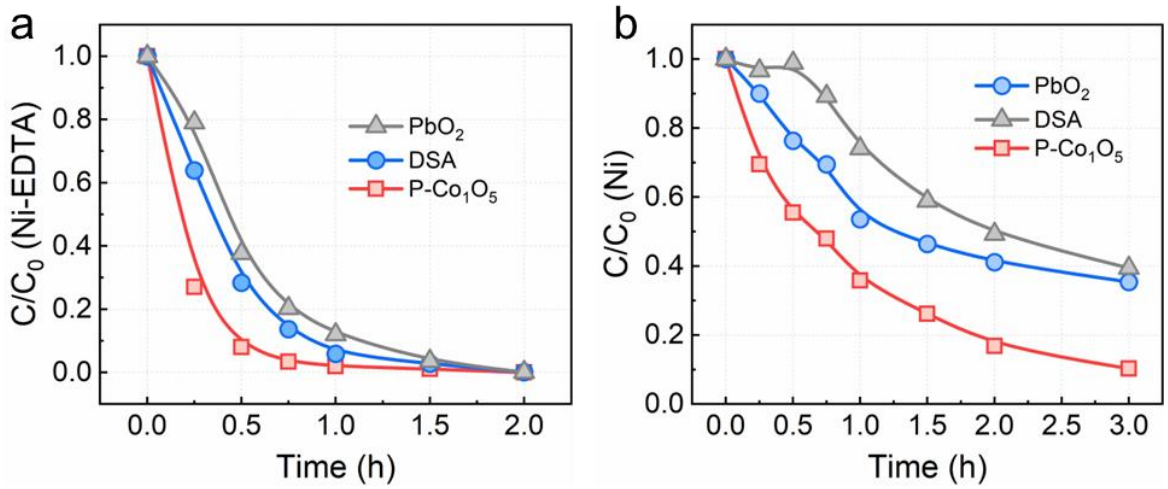

Supplementary Figure S31. (a) Ni-EDTA decomplexation and (b) corresponding Ni removal performance by PbO_2, DSA and P-Co_1O_5 electrodes.

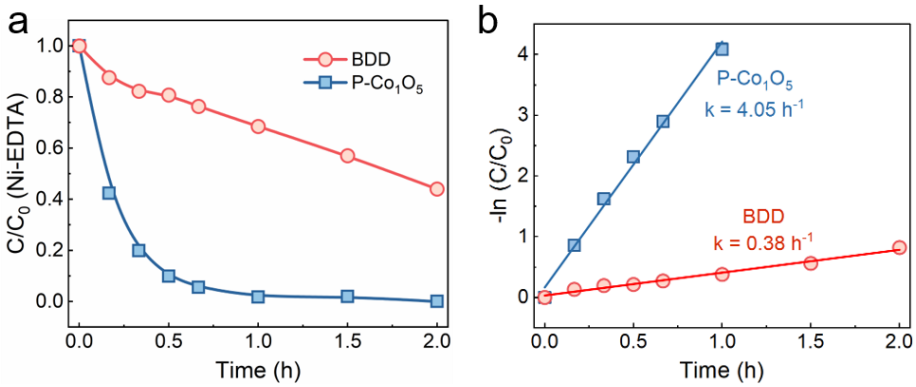

Supplementary Figure S32. (a) Ni-EDTA decomplexation efficiency and (b) Corresponding observed reaction rate constants for commercial BDD and P-Co_1O_5 electrodes.

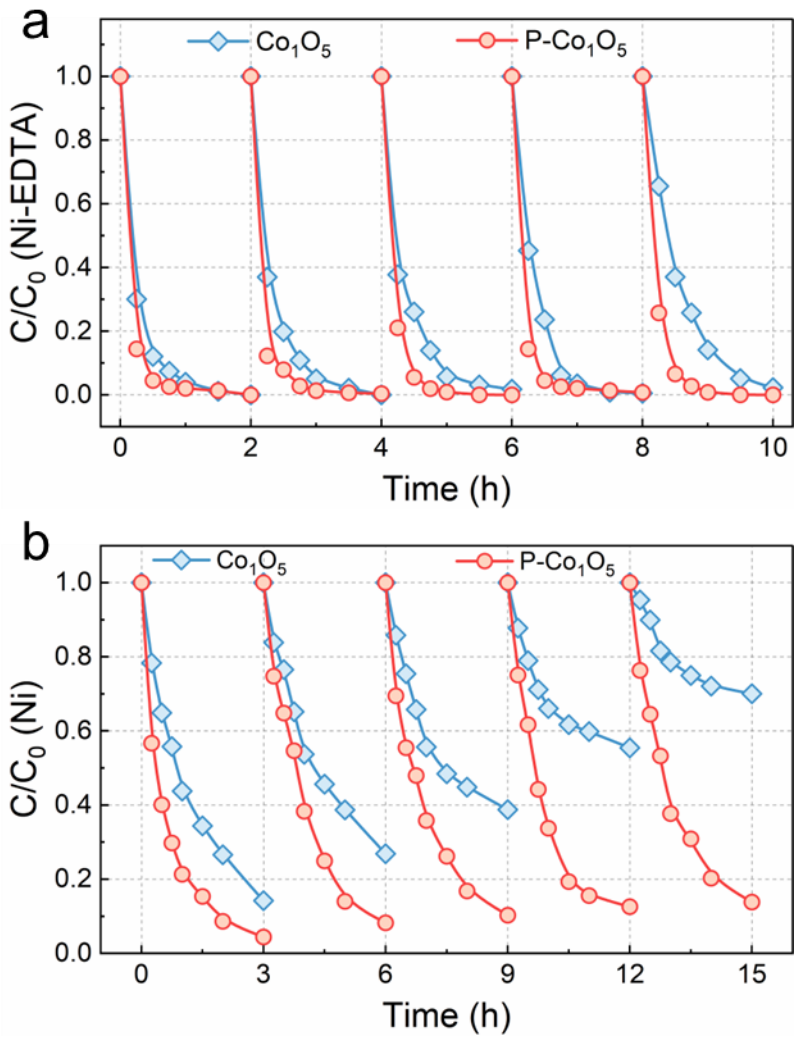

Supplementary Figure S33. (a) The Ni-EDTA decomplexation and (b) Ni removal efficiency performance of Co_1O_5 and P-Co_1O_5 during the stability tests.

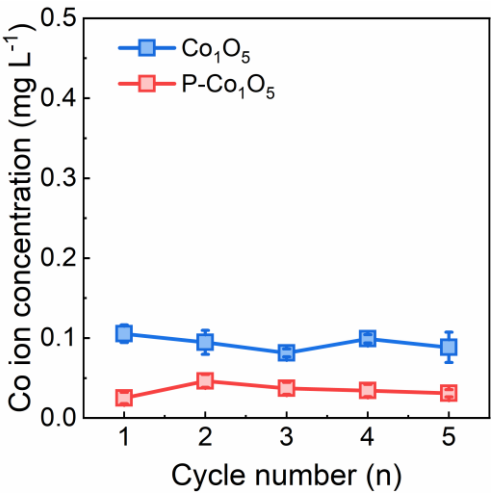

Supplementary Figure S34. Concentration of dissolved Co of Co_1O_5 and P-Co_1O_5 during the five cycle tests.

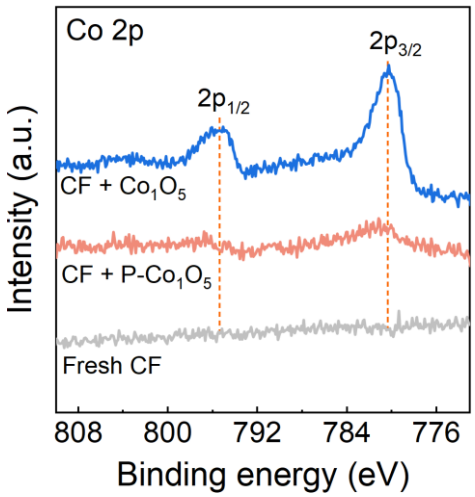

Supplementary Figure S35. Comparison of high-resolution Co 2p XPS spectra of the fresh carbon felt (CF) and after five cycles of decomplexation by Co_1O_5 and P-Co_1O_5.

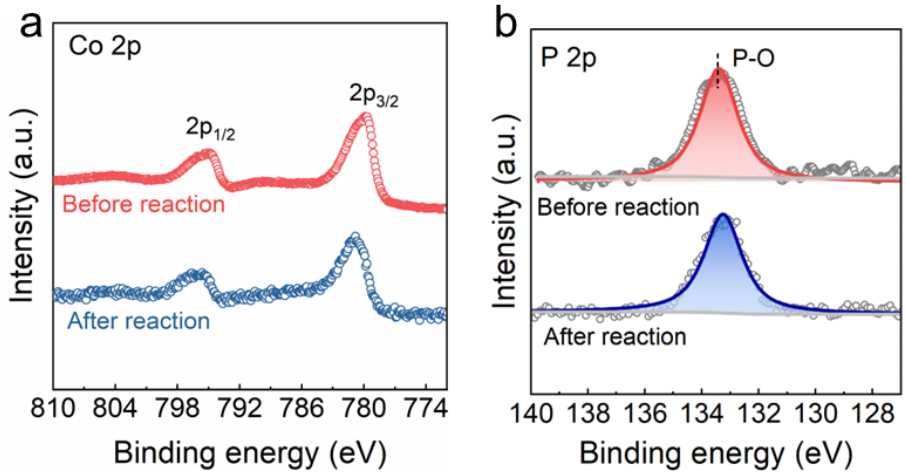

Supplementary Figure S36. High-resolution (a) Co 2p and (b) P 2p XPS spectra of P-Co_1O_5 before and after stability tests.

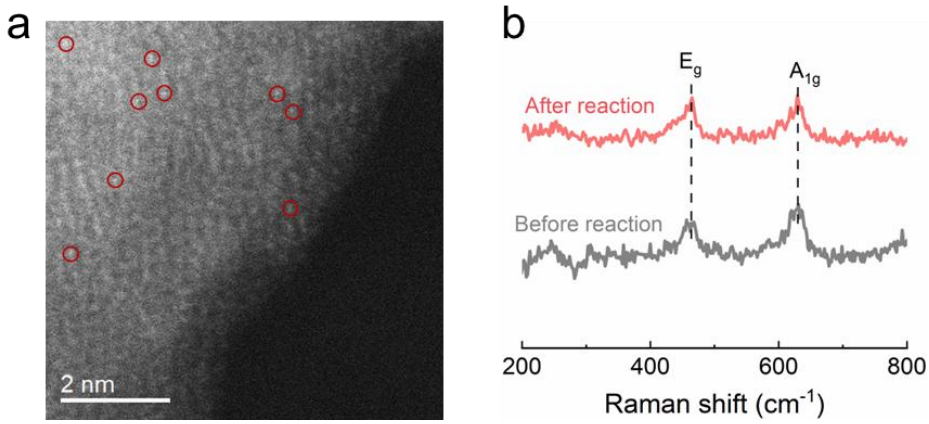

Supplementary Figure S37. (a) AC HADDF-STEM image of P-Co_1O_5 after reaction. (b) Raman spectra of P-Co_1O_5 before and after reaction.

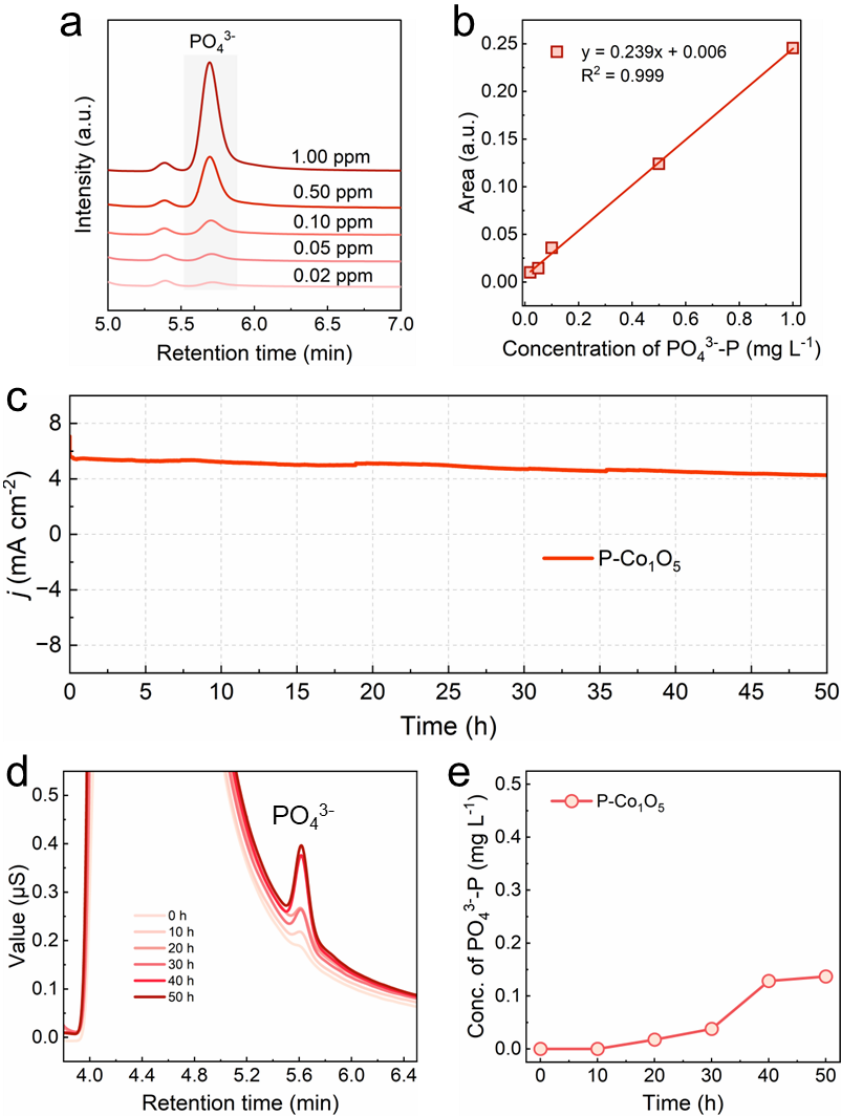

Supplementary Figure S38. (a) Ion chromatography (IC) curves of PO_4^{3-} at different concentrations. (b) Corresponding calibration curve for PO_4^{3-} quantification. (c) Long-term durability performance of the P-Co_1O_5 electrode at 2.1 V vs. RHE. (d) IC curves recorded at different electrolysis times. (e) Leached concentration of PO_4^{3-} from P-Co_1O_5 as a function of electrolysis time.

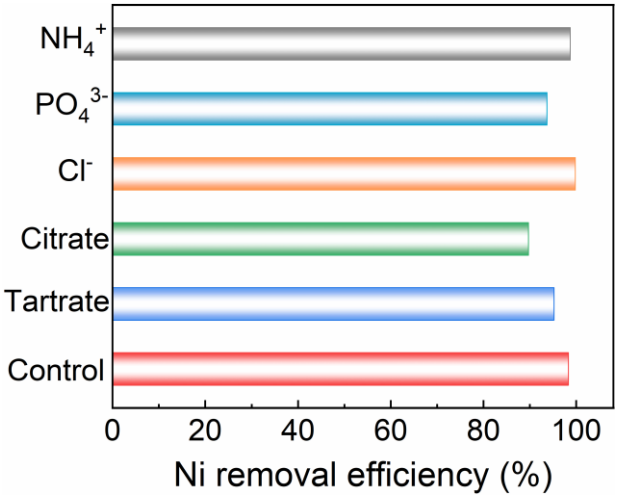

Supplementary Figure S39. Effect of various background substances (anions, cations, and organic matter) on the decomplexation of Ni-EDTA by P-Co_1O_5. The concentration of Ni-EDTA and coexisting substances were 10 and 50 mg L^{-1}, respectively. The applied potential was 2.1 V vs. RHE.

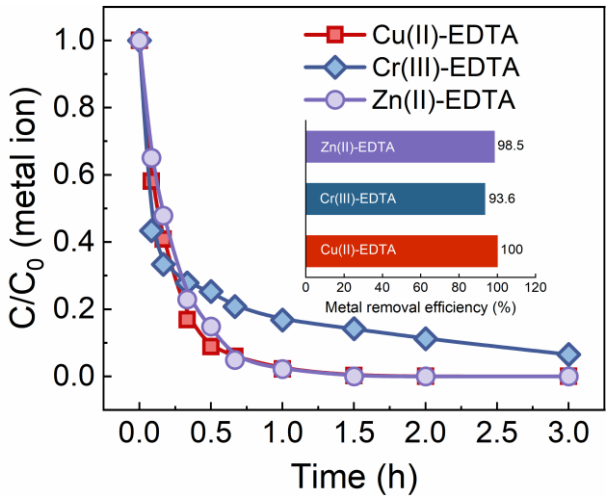

Supplementary Figure S40. Electrochemical decomplexation of Cu(II)-EDTA, Cr(III)-EDTA and Zn(II)-EDTA (10 mg L^{-1} each) by P-Co_1O_5 at 2.1 V vs. RHE.

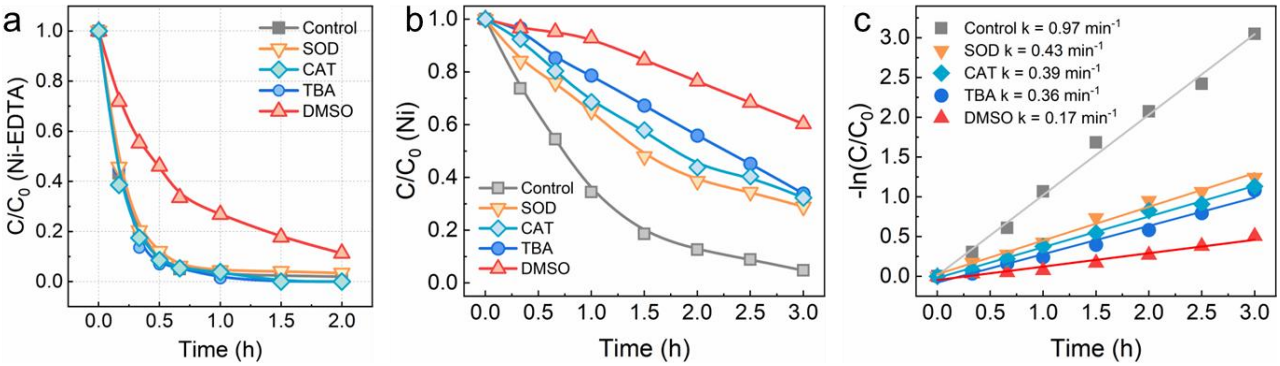

Supplementary Figure S41. (a) The inhibition effect of Ni removal in the presence of various scavengers in P-Co_1O_5.

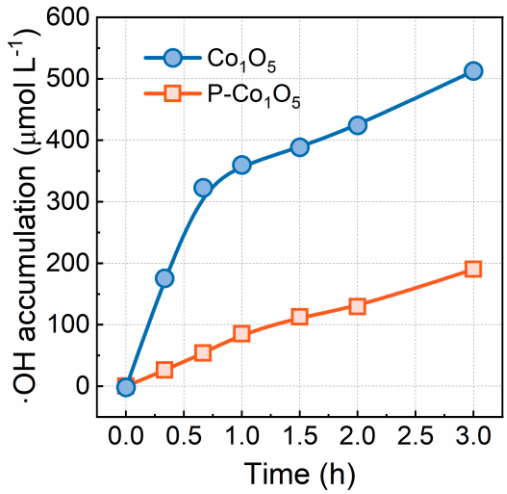

Supplementary Figure S42. The concentration of ·OH generated by Co_1O_5 and P-Co_1O_5.

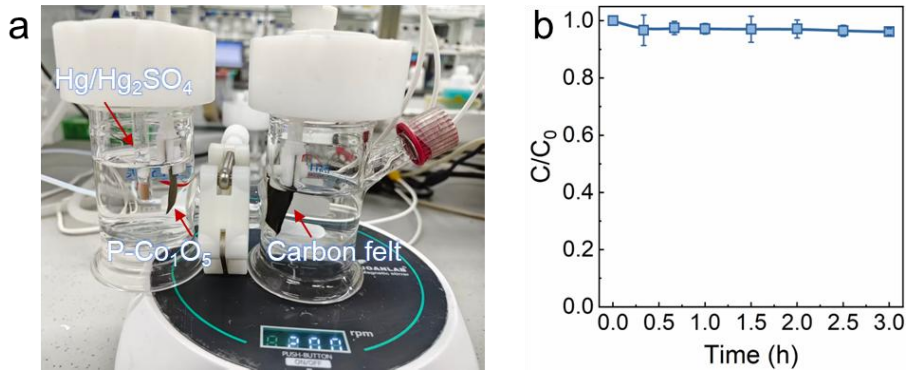

Supplementary Figure S43. (a) Photograph of the H-type electrolysis reactor. (b) Ni removal efficiency using a carbon felt cathode at 2.1 V vs. RHE.

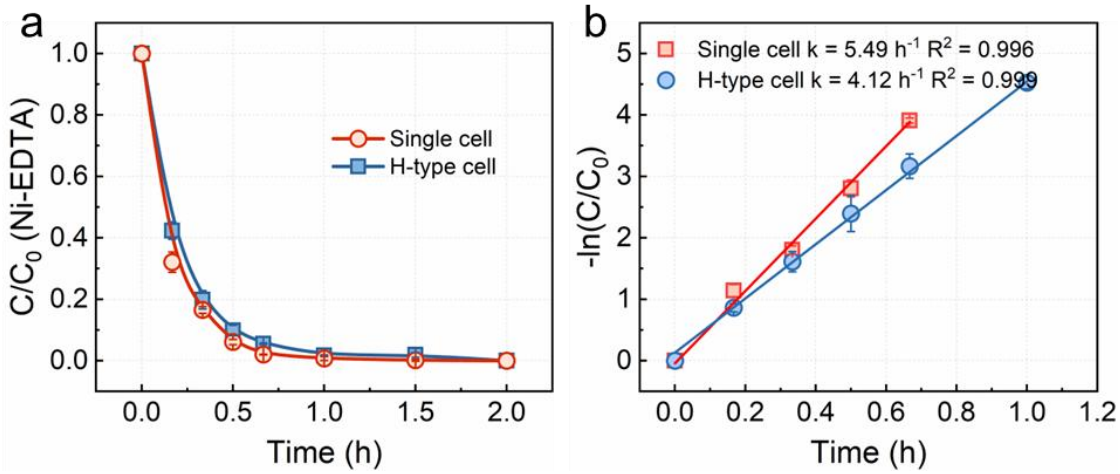

Supplementary Figure S44. Comparison between single cell and H-type cell configurations for Ni-EDTA decomplexation using P-Co_1O_5. (a) Ni-EDTA decomplexation efficiency and (b) the observed reaction rate constants.

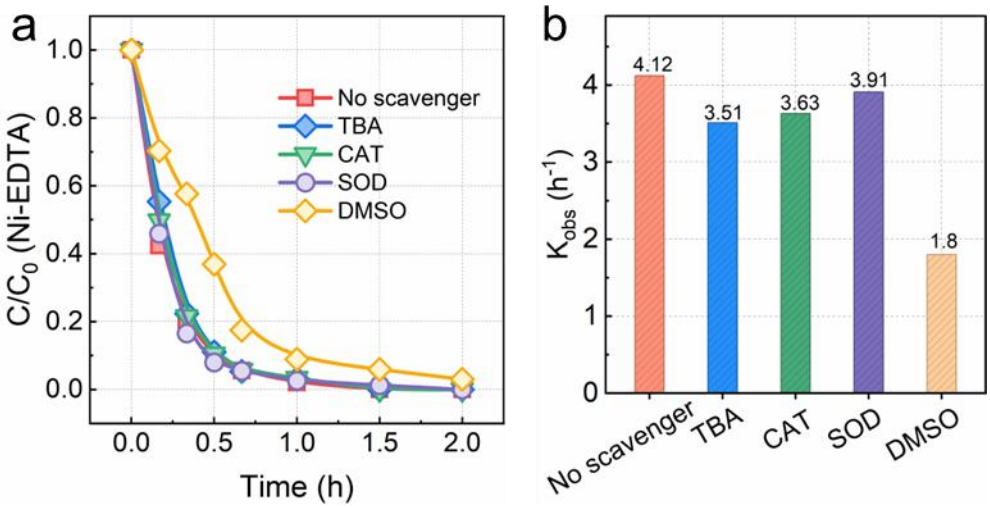

Supplementary Figure S45. The inhibition effect of Ni-EDTA decomplexation in the presence of various scavengers in P-Co_1O_5 in H-type cell. (a) Ni-EDTA decomplexation efficiency and (b) the corresponding observed reaction rate constants under various scavengers.

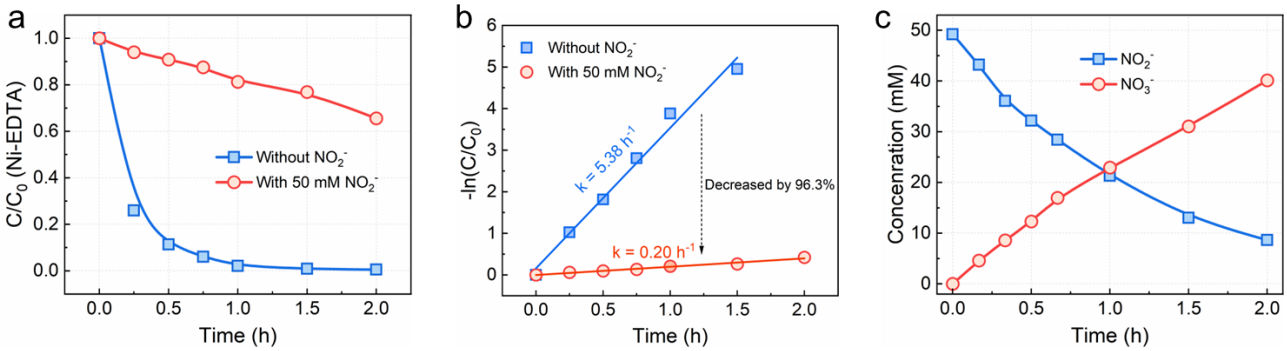

Supplementary Figure S46. (a) Effect of NO_2^- on the Ni-EDTA decomplexation by P-Co_1O_5 in H-type cell. (b) Corresponding observed reaction rate constants with and without 50 mM NO_2^- in single cell. The concentration of (c) NO_2^- and NO_3^-.

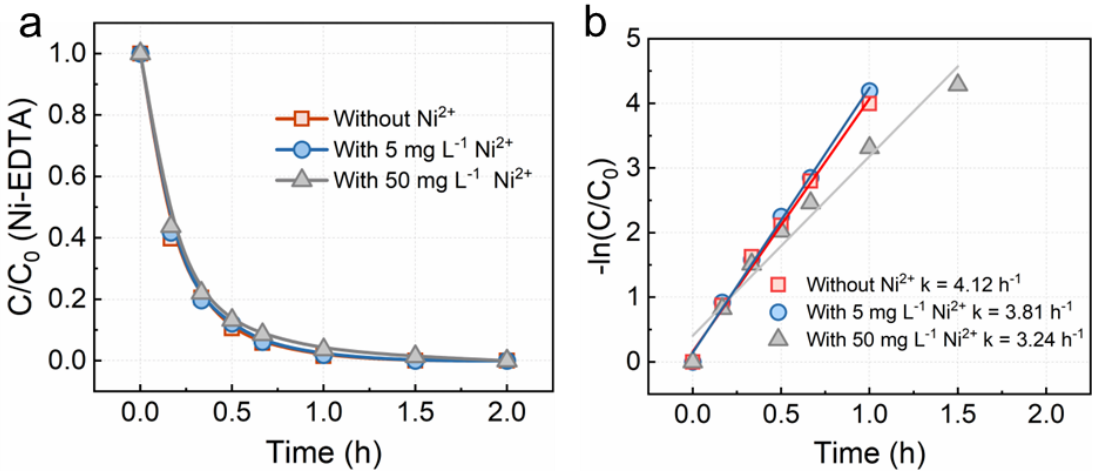

Supplementary Figure S47. Effect of exogenous Ni^{2+} addition on Ni-EDTA decomplexation using P-Co_1O_5. (a) Ni-EDTA decomplexation efficiency and (b) the corresponding observed reaction rate constants under different Ni^{2+} concentration.

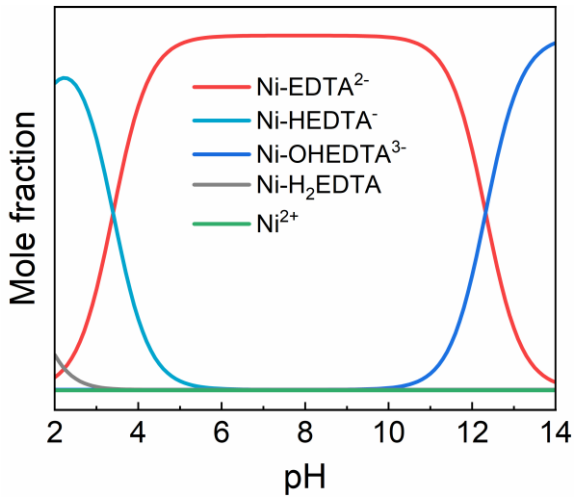

Supplementary Figure S48. Distribution of Ni-EDTA species with pH variation.

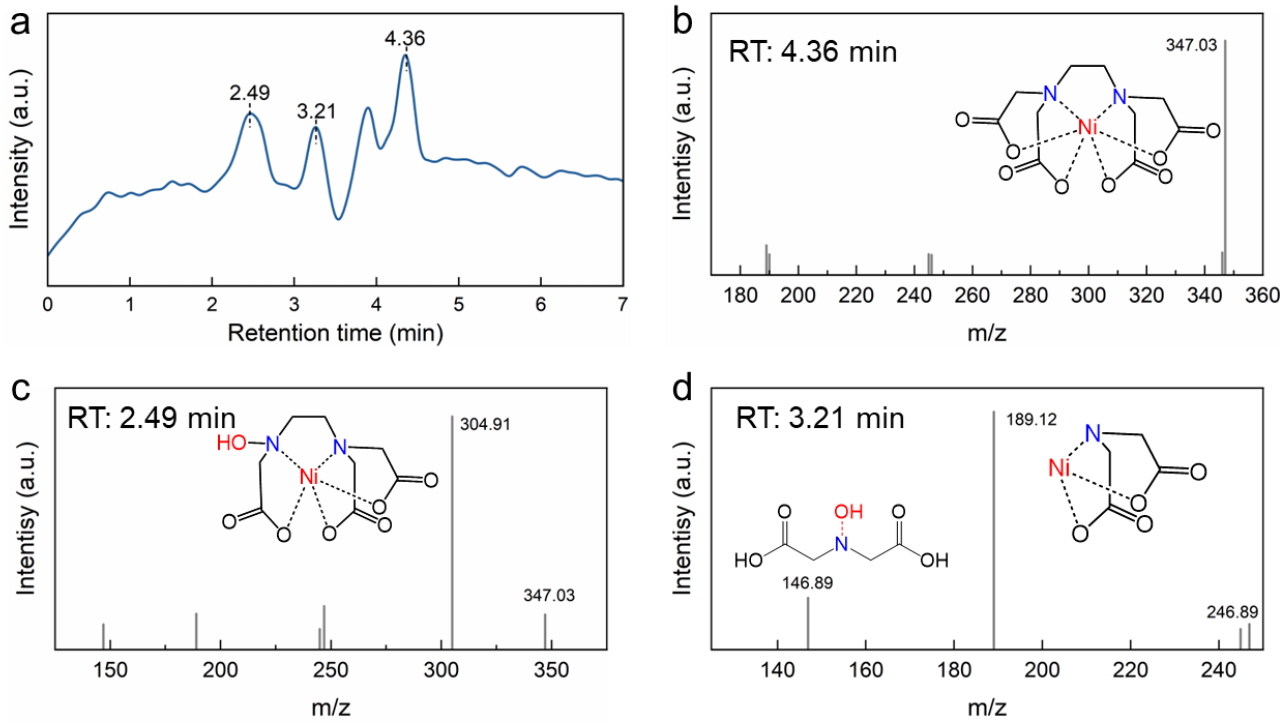

Supplementary Figure S49. (a) The extracted HPLC chromatogram. Mass spectra of Ni-EDTA decomplexation intermediates of (b) Ni-EDTA (m/z = 347.03 $[M-H]^-$), (c) Ni-ED3A-OH (m/z = 304.91 $[M-H]^-$), (d) IDMA-OH (m/z = 146.89 $[M-H]^-$) and Ni-IDMA (m/z = 189.12 $[M-H]^-$).

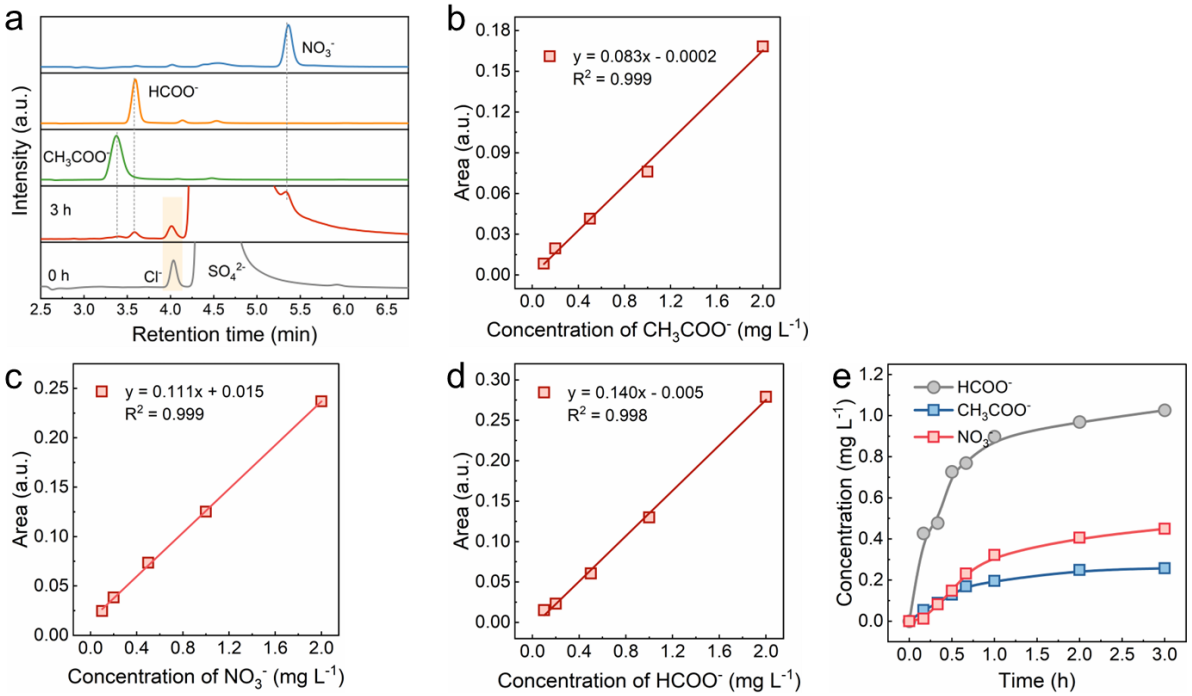

Supplementary Figure S50. (a) Ion chromatography (IC) profiles of the electrolyte at 0 h and 3 h in an H-type electrolysis cell, together with $HCOO^-$, CH_3COO^- and NO_3^- standards. Corresponding calibration curves for quantification of (b) CH_3COO^- (c) NO_3^- and (d) $HCOO^-$. (e) Concentrations of $HCOO^-$, CH_3COO^- and NO_3^- during 3 h electrolysis at 2.1 V vs. RHE in an H-type electrolysis cell.

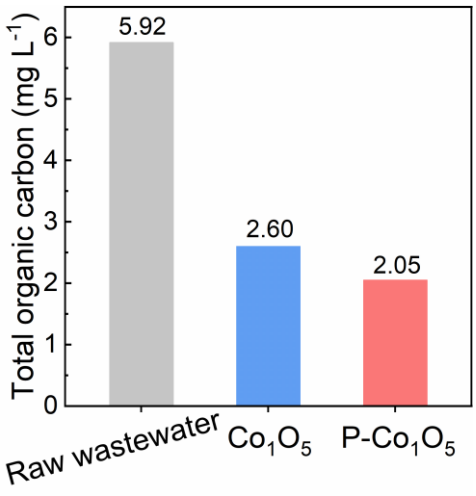

Supplementary Figure S51. Concentration of total organic carbon (TOC) before and after treatment with Co_1O_5 and P-Co_1O_5.

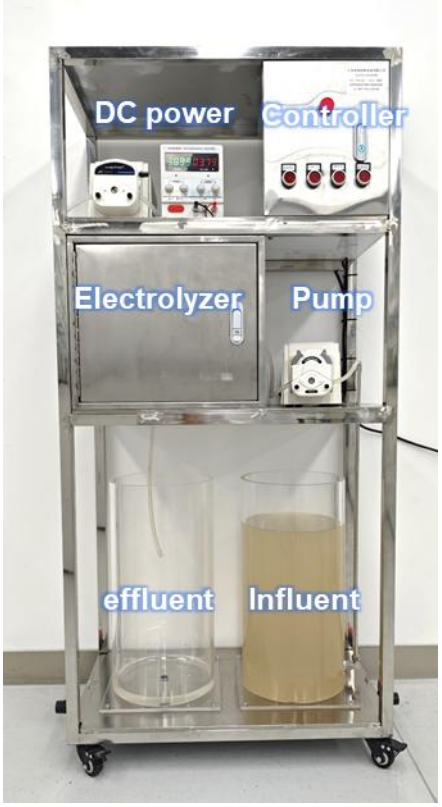

Supplementary Figure S52. (a) Photograph of the pilot-scale electrochemical oxidation coupled reduction (EOCR) device for decomplexation.

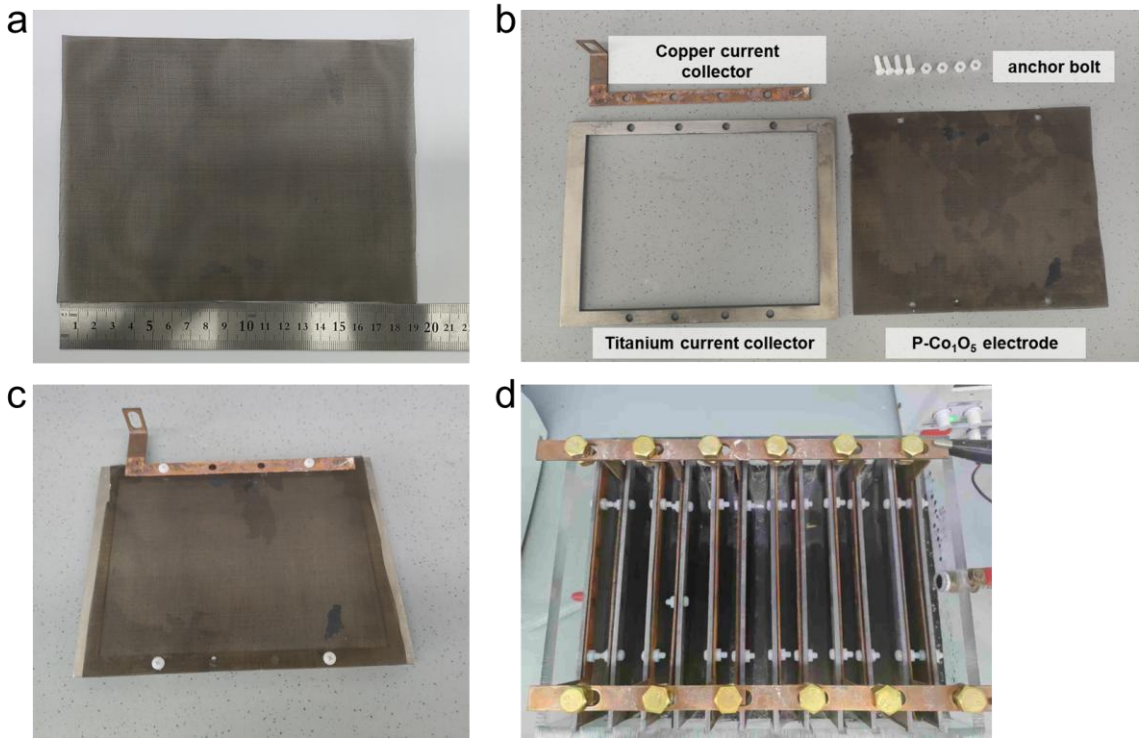

Supplementary Figure S53. Assembly process of the EOCR electrolyzer. Images showing (a) P-Co_1O_5 electrode (193 * 140 mm^2), (b) The components for electrode assembly, (c) the assembly of the P-Co_1O_5 electrode and (d) the fully assembled EOCR electrolyzer.

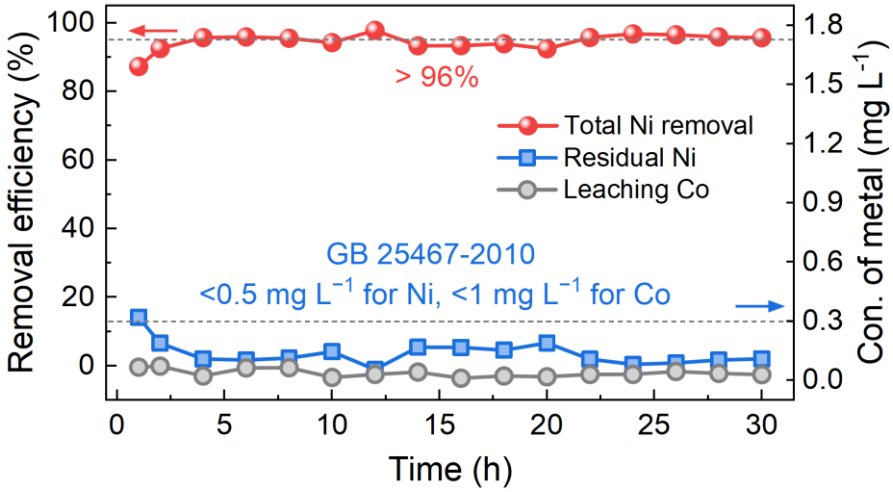

Supplementary Figure S54. Total Ni removal efficiency and concentration of residual Ni and leaching Co during the treatment of Ni-EDTA simulated wastewater. The operational conditions were a flow rate of 2.5 L h^{-1} and a current of 3.9 A.

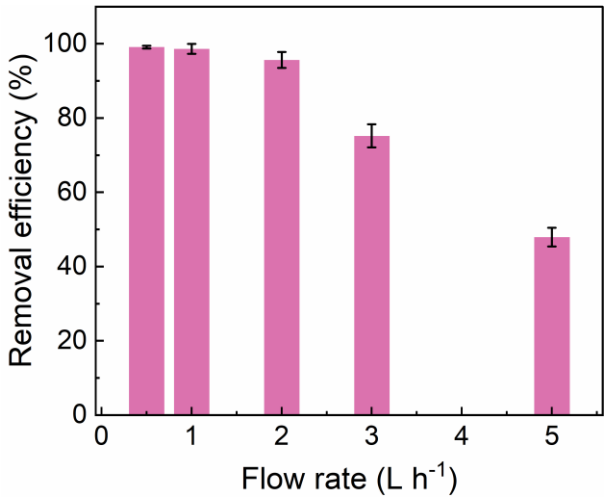

Supplementary Figure S55. Ni removal efficiency at different flow rate of real wastewater with a current of 3.9 A.

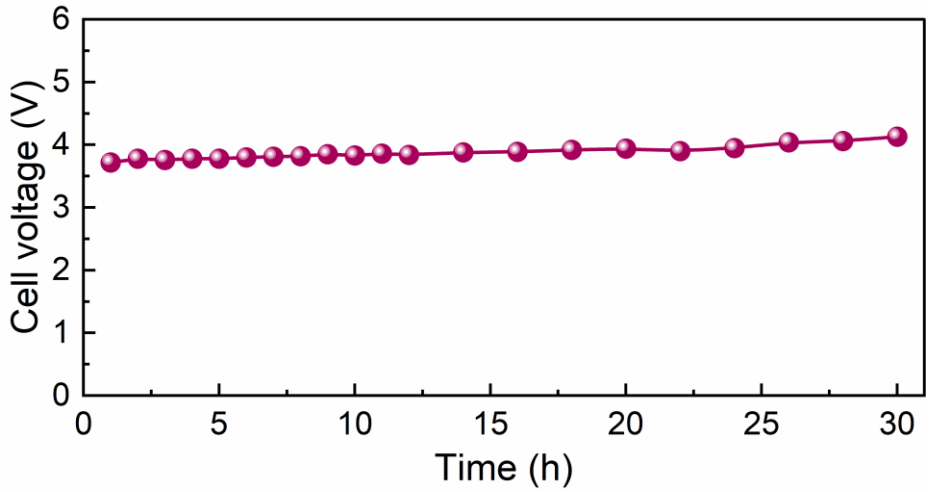

Supplementary Figure S56. Cell Voltage of EOCR device during the continuous treatment of real wastewater.

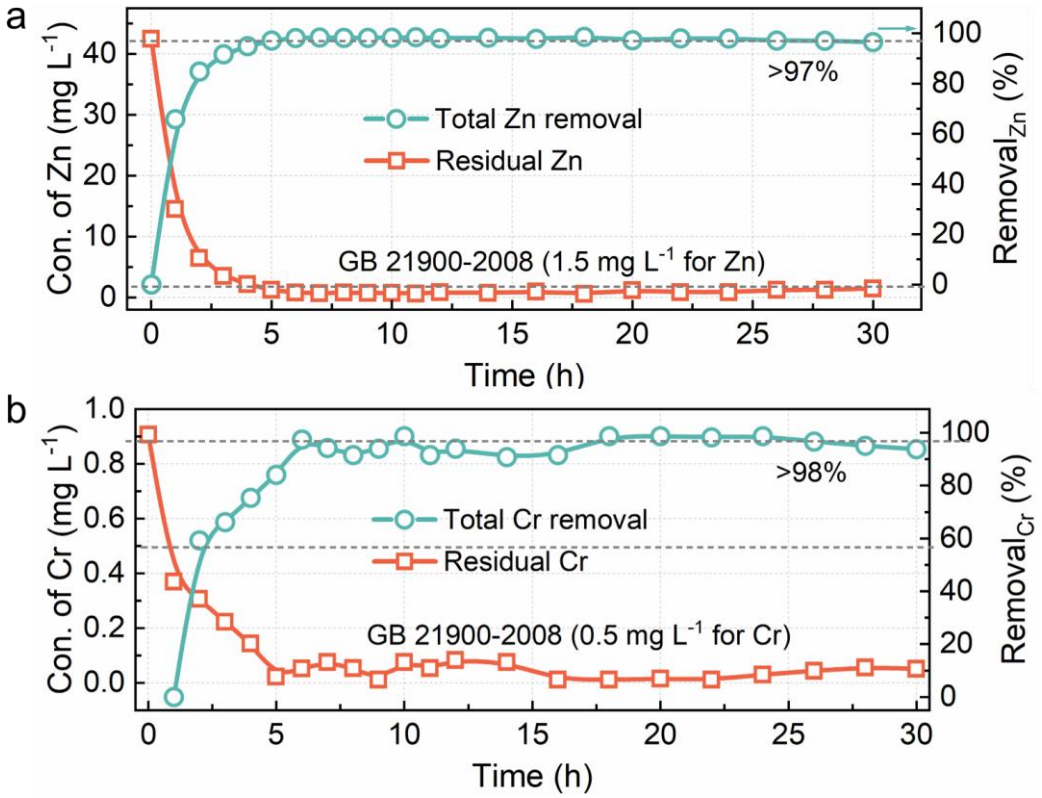

Supplementary Figure S57. The concentration and corresponding total removal efficiency of (a) Zn and (b) Cr in effluent during continuous treatment of real electroplating wastewater.

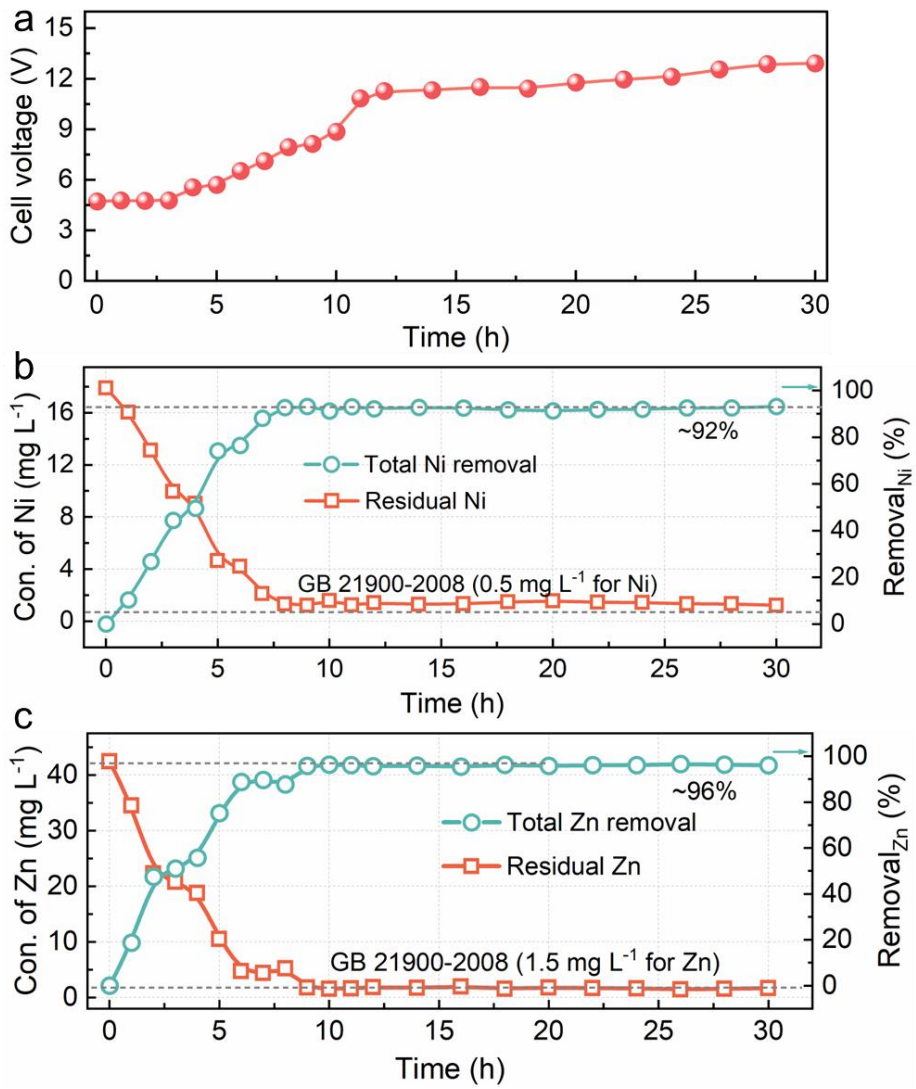

Supplementary Figure S58. (a) Cell voltage of EOCR device based on the Co_1O_5 anode during the continuous treatment of real wastewater. The concentration and corresponding total removal efficiency of (b) Ni and (c) Zn in effluent during continuous treatment of real electroplating wastewater.

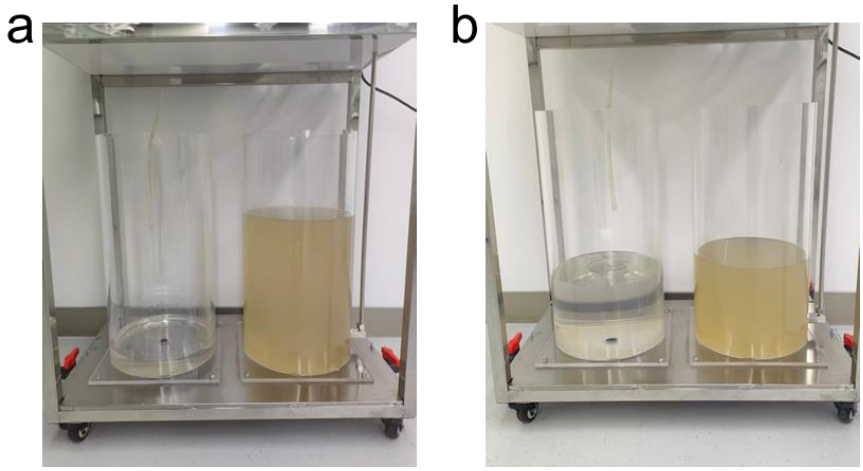

Supplementary Figure S59. Photographs showing the color change of the wastewater from influent to effluent after 1 h (a) and 4 h (b) of treatment by EOCR device.

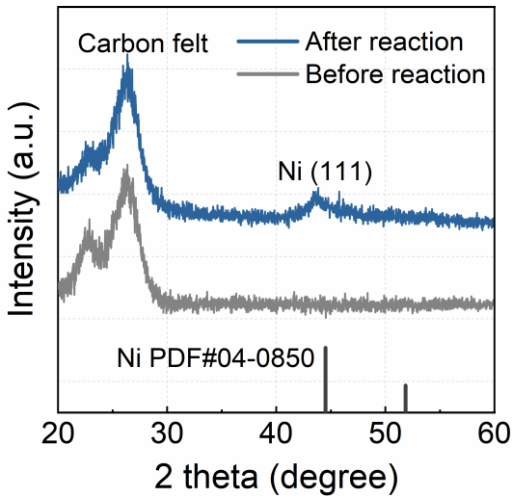

Supplementary Figure S60. XRD patterns of the carbon felt before and after reaction.

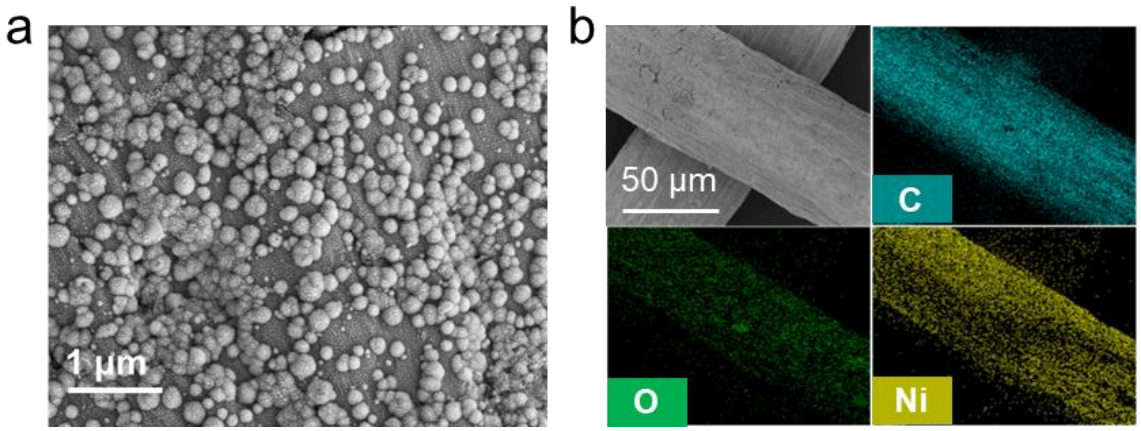

Supplementary Figure S61. (a) SEM images and (b) corresponding EDS mapping of carbon felt after reaction.

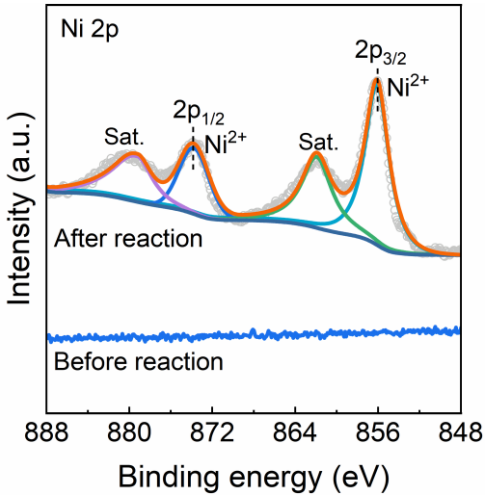

Supplementary Figure S62. High-resolution Ni 2p XPS of carbon felt before reaction and after reaction.

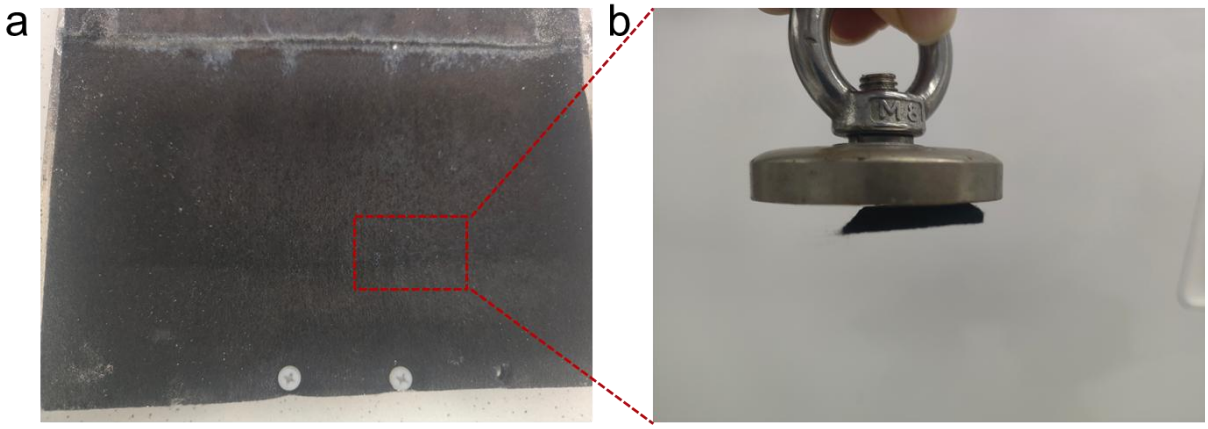

Supplementary Figure S63. Carbon felt cathode (a) after reaction and (b) attracted by a magnet.

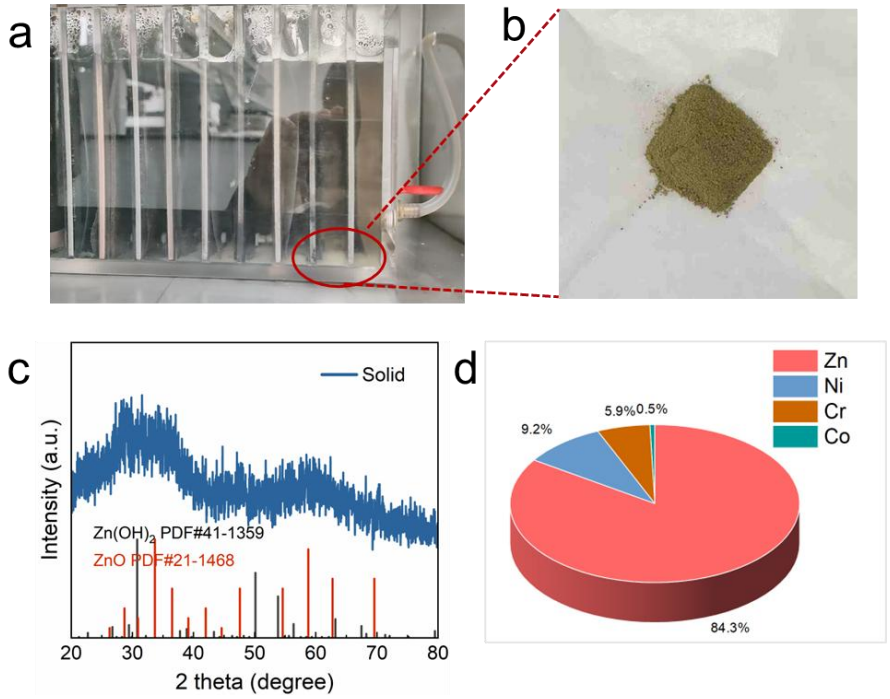

Supplementary Figure S64. (a) Photograph of the EOCR electrolyzer during the treatment of real wastewater, showing white precipitate at the bottom. (b) Photograph of the precipitate after filtration and drying at 80 ℃ overnight. (c) XRD pattern of the recovered solid. (d) Corresponding metal quantification analysis determined by ICP-OES.

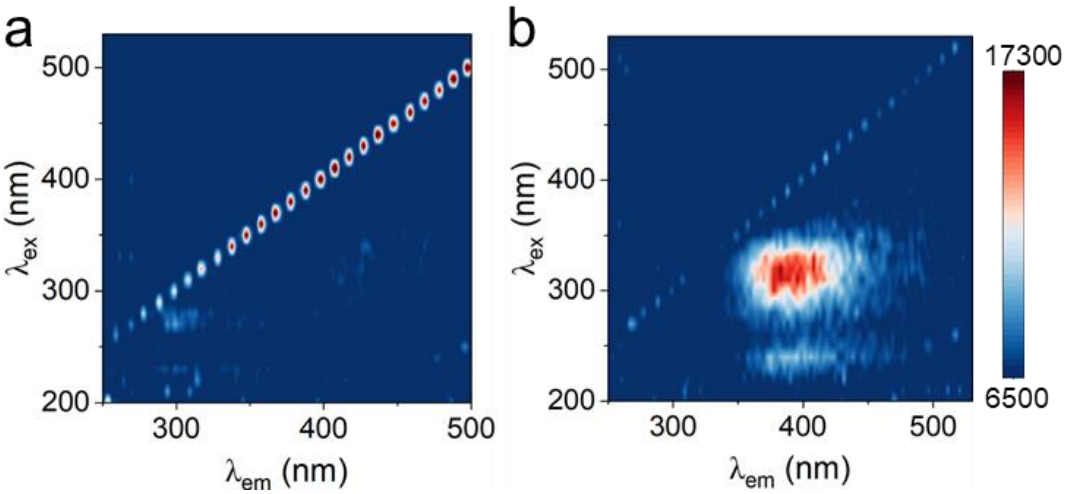

Supplementary Figure S65. 3D EEM fluorescence spectra of real metal-complex wastewater (a) in the influent and (b) in the effluent.

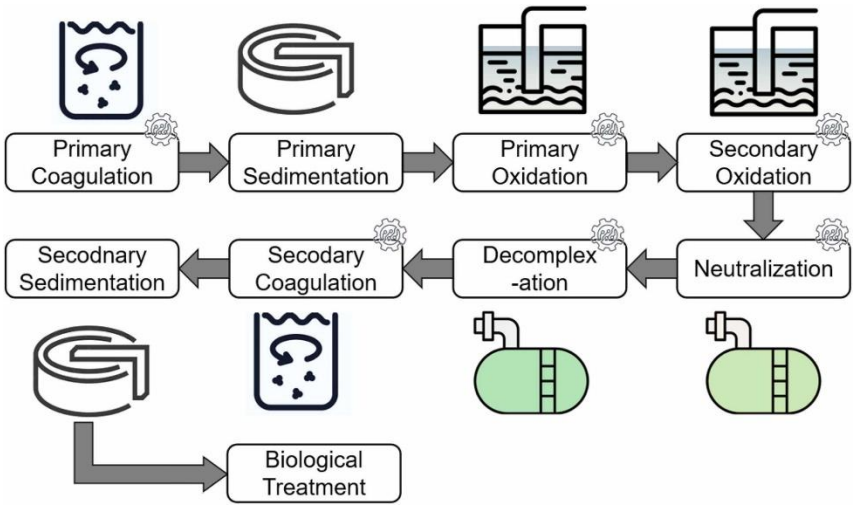

Supplementary Figure S66. Conversion muti-stage physicochemical treatment (MSPT) processes for the mixed electroplating wastewater[9].

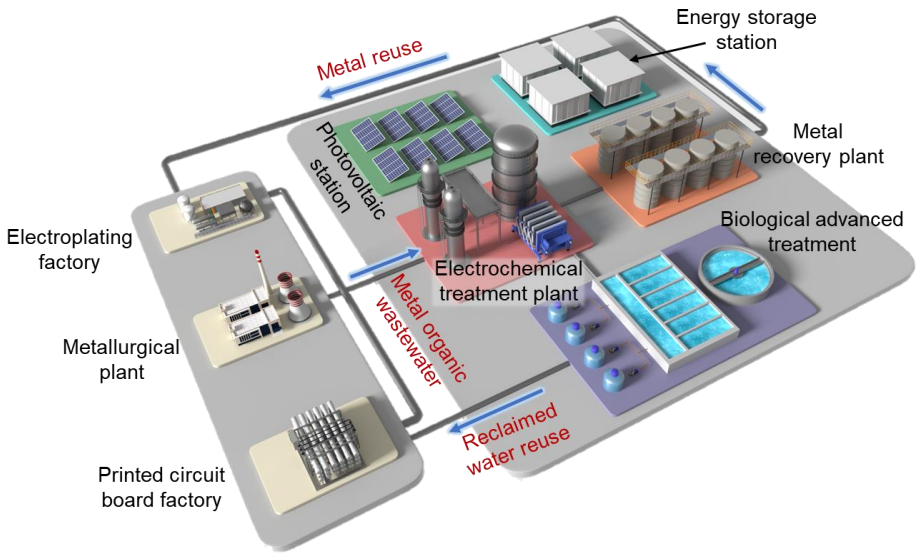

Supplementary Figure S67. Schematic of the renewable energy-driven electrochemical oxidation coupled reduction (EOCR) process for green and resource-recovery treatment of metal-containing wastewater.

Supplementary Figure S68. Photograph of a large-scale P-Co_1O_5 monolithic electrode (75 cm × 50 cm) before annealing treatment.

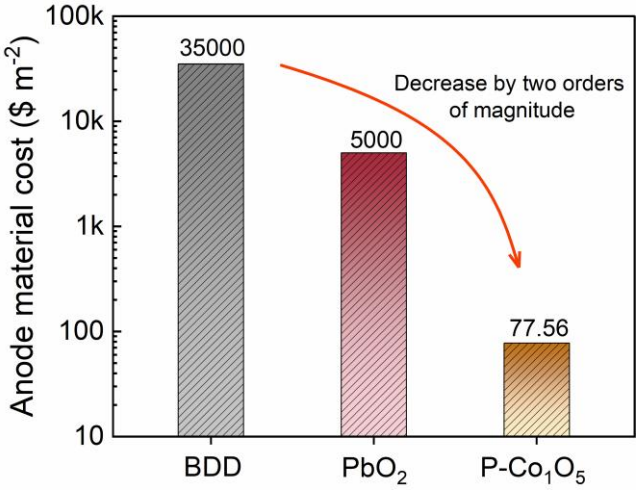

Supplementary Figure S69. Cost comparison of BDD, PbO_2 and P-Co_1O_5 anodes[10].

Supplementary Table S2. ICP-MS results of Co_1O_5 and P-Co_1O_5.

Catalysts	Element	Mass concentration (wt%)	Atomic concentration (%)
Co_1O_5	Co	0.121	
P-Co_1O_5	Co	0.110	0.00188
	P	0.0553	0.00179

Supplementary Table S3. EXAFS fitting parameters at the Co K-edge for various samples.

	shell	CN[a]	R[b](Å)	σ^{2c}(Å^2)	$\Delta E_0{}^d$(eV)	R factor
Co foil	Co–Co	12	2.49 ± 0.01	0.0059	-1.9 ± 0.5	0.0021
	Co–O	6.3 ± 0.4	1.91 ± 0.01	0.0032		
Co_3O_4	Co–Co	4.8 ± 0.2	2.85 ± 0.01	0.0034	-7.3 ± 0.6	0.0055
	Co–Co	5.9 ± 0.6	3.37 ± 0.01	0.0070		
P-Co_1O_5	Co–O	5.1 ± 0.5	2.05 ± 0.02	0.0053	2.5 ± 2.1	0.0153
Co_1O_5	Co–O	4.8 ± 0.7	2.00 ± 0.02	0.0142	0.04 ± 1.4	0.0061

[a]*CN*, coordination number; [b]*R*, distance between absorber and backscatter atoms; [c]σ^2, Debye-Waller factor to account for both thermal and structural disorders; [d]ΔE_0, inner potential correction; *R* factor indicates the goodness of the fit. $S_0{}^2$ was fixed to 0.67, according to the experimental EXAFS fit of Co foil by fixing CN as the known crystallographic value. A reasonable range of EXAFS fitting parameters: $0.600 < S_0{}^2 < 1.000$; $CN > 0$; $\sigma^2 > 0$ Å^2; $|\Delta E_0| < 15$ eV; *R* factor < 0.02.

Supplementary Table S3. The fitting results of EIS plots of Ti mesh, P-Ti, Co_1O_5 and P-Co_1O_5.

Electrode	R_s (R)	R_{ct} (R)
Ti mesh	3.72	127.4
P-Ti	3.87	72.9
Co_1O_5	4.37	29.8
P-Co_1O_5	4.10	5.8

Supplementary Table S4. Comparative analysis of Co^{IV}=O performance among different activation processes.

Methods to generate Co^{IV}=O	Materials	Co^{IV}=O yield (mmol L^{-1} h^{-1})	Refs.
PMS activation	Co-OCN	0.028	[11]
	Co_4Cu_1-LDH	0.035	[12]
	CoN_1O_2/Mn_3O_4	0.025	[13]
	Co-TiO_2	0.050	[14]
	CoPC-SO_3H	0.080	[15]
	CoN_4–O–CuN_4	~0.120	[16]
ClO_2^- activation	OV-Co_3O_4	0.060	[17]
	Co_3O_4	0.070	[18]
PAA activation	Co(II)	0.185	[19]
	Co doped C_3N_4	0.145	[20]
Electrochemical water oxidation	Co_1O_5	0.28	This work
	P-Co_1O_5	0.49	

Supplementary Table S5. Real wastewater parameters sampled from a electroplate park (Zhejiang, China).

Effluent	Ni mg L^{-1}	Zn mg L^{-1}	Cr mg L^{-1}	Co mg L^{-1}	Conductivity mS cm^{-1}	COD mg L^{-1}	pH
	17.8	44.2	0.97	0.13	3.61	1098	11.14

Supplementary Table S6. Comparative analysis of Ni removal efficiency and energy efficiency for Ni-EDTA treatment under different conditions reported in the literatures.

Electrode materials	$C_{0,\ Ni\text{-}EDTA}$ (mM)	Treatment capacity (L)	$R_{Ni\ removal}$ (%)	$E_{removal}$ (g kWh^{-1})	EEO (kWh m^{-3})	Refs.
PbO_2	1	72	74	7.9	13.6	[10]
Bi-PbO_2	1	-	66	-	13.98	[21]
Ni-PbO_2	1	0.2	52	5.82	2.6	[22]
Ti^{3+}-doped TiO_2	0.2	0.07	71	1.66	-	[23]
Fe	0.0232	0.45	94	1.51	-	[24]
RuO_2-IrO_2/Ti /Fe	4.79	0.5	94	4.46	-	[25]
Carbon felt	10	0.03	95.5	-	35.31	[26]
Ni-doped red mud	0.1	0.1	90	-	7.62	[27]
Fe-N-RHBC	0.128	0.1	94.1	-	-	[28]
Dual mixed metal oxide /Fe	0.68	0.25	94.2	3.45	16.36	[29]
P-Co_1O_5	17.8 mg/L Ni 44.2 mg/L Zn	60	~97% for Zn ~95% for Ni	8.64	5.85	This work
Co_1O_5		60	~96% for Zn ~92% for Ni	2.93	18.28	

Supplementary Table S7. Technoeconomic analysis of MSPT process. Data on the main costs, including chemical reagents, sludge treatment, and electricity, were collected from the literature[9]. Technoeconomic analysis of EOCR process was presented in Text S8.

Annual data	1	2	3
Wastewater consumption (m^3)	66934	97332	59987
Average cost of chemical reagents (￥/m^3)	17.287	15.970	15.444
Unit cost of chemical reagents over the three years (￥/m^3)		16.222	
Unit sludge treatment cost (￥/ton)	39.642	40.162	37.875
Unit sludge treatment cost over the three years (￥/ton)		39.226	
Electricity consumption (kWh/m^3)	4.535	3.915	3.910
Unit electricity consumption over the three years (kWh/m^3)		4.120	
According to the exchange rate of USD ($) to RMB (￥): one USD to 7.1 RMB			
Average cost of chemical reagents ($/$m^3$)		2.285	
Unit sludge treatment cost over the three years ($/ton)		5.525	
Unit electricity consumption cost over the three years (kWh/m^3)		0.288	
Total cost (kWh/m^3)		8.098	

Supplementary Table S8. Life cycle assessment inventory for the treatment of 1 kg of complexed heavy metal in wastewater by the MSPT and EOCR processes.

MSPT		Inventory name	Quantity	Unit
Input	**Materials**	$Na_2S_2O_5$	1116.331	g
		PAC	347.443	g
		NaOH	42.328	g
		APAM	63.492	g
		Na_2S	317.460	g
		NaClO	19.400	g
		Lime	3.527	g
		H_2SO_4	1439.153	g
		$FeSO_4$	620.811	g
		H_2O_2	130.511	g
		30% NaOH	21.164	g
		Water	16.13	m^3
		Glucose	183.422	g
	Energy	Electricity	4.933	kWh
Output	**Materials**	Water	16.13	m^3
		Sludge	19.474	kg

LCA of EOCR process including electrode fabrication, wastewater treatment and metal recovery

EOCR-Co electrode fabrication		Inventory name	Quantity	Unit
Input	Materials	$Co(NO_3)_2·6H_2O$	0.3201	g
		NaH_2PO_2	0.3692	g
		Ethanol	65	mL
		Water	130	mL
		Titanium mesh	325	g
		Nitrogen	18	L
	Energy	Electricity	5	kWh
Output	Waste to be disposed of	Gas	18	L
	Waste to be disposed of	Solid	0.1	g

EOCR Process for wastewater treatment				
Input	Materials	Co electrode	325	g
		Carbon felt	300	g
		Water	16.13	m^3
	Energy	Electricity	120.4	kWh
Output	Waste to be recovered	Co electrode	32.5	g
	Waste to be recovered	Carbon felt	30.0	g
EOCR Process for metal recovery				
Input	Materials	HCl	325	g
		Water	5	L
	Energy	Electricity	1.0	kWh
Output	Waste to be recovered	$NiCl_2$	640.35	g
	Waste to be recovered	$Zn(OH)_2$ /ZnO	1096.31	g
	Waste to be disposed of	Water	5.0	L

Supplementary Table S9. The usage of the chemicals, materials and energy in fabricating 1 m^2 P-Co_1O_5 anode

Chemicals and materials	Unit price	Usage	Cost
$Co(NO_3)_2 \cdot 6H_2O$	36.06 \$ kg^{-1}	0.3201 g	0.012 \$
NaH_2PO_2	20.11 \$ kg^{-1}	0.3692 g	0.007 \$
Ethanol	6.22 \$ kg^{-1}	65 g	0.403 \$
Water	0.8 \$ ton^{-1}	130 g	Negligible
Nitrogen	0.51 \$ L^{-1}	18 L	9.18 \$
Titanium mesh	67.61 \$ m^{-2}	1 m^2	67.61 \$
Electricity	0.07 \$ kWh^{-1}	5 kWh	0.35 \$
Total cost			77.56 \$

References

[1] Leow, W. R.; et al. Chloride-mediated selective electrosynthesis of ethylene and propylene oxides at high current density. *Science* **2020**, *368* (6496), 1228-1233.

[2] Cai, L.; et al. Atomically Asymmetrical Ir−O–Co Sites Enable Efficient Chloride-Mediated Ethylene Electrooxidation in Neutral Seawater. *Angew. Chem., Int. Ed.* **2025**, *64* (5), e202417092.

[3] Hafner, J. Ab-initio simulations of materials using VASP: Density-functional theory and beyond. *Journal of Computational Chemistry* **2008**, *29* (13), 2044-2078.

[4] Perdew, J. P.; et al. Generalized Gradient Approximation Made Simple. *Phys. Rev. Lett.* **1996**, *77* (18), 3865-3868.

[5] Li, L.; et al. Imaging Catalytic Activation of CO_2 on Cu_2O (110): A First-Principles Study. *Chem. Mater.* **2018**, *30* (6), 1912-1923.

[6] Hu, Y.; et al. Single Ru Atoms Stabilized by Hybrid Amorphous/Crystalline FeCoNi Layered Double Hydroxide for Ultraefficient Oxygen Evolution. *Adv. Energy Mater.* **2021**, *11* (1), 2002816.

[7] Kunitski, M.; et al. Double-slit photoelectron interference in strong-field ionization of the neon dimer. *Nat. Commun.* **2019**, *10* (1), 1.

[8] Tian, F.; et al. Raman Spectroscopy: A New Approach to Measure the Percentage of Anatase TiO_2 Exposed (001) Facets. *J. Phys. Chem. C.* **2012**, *116* (13), 7515-7519.

[9] Gao, J.; et al. Navigating challenges in electroplating wastewater management: A study on pollutant removal characteristics and economic impacts by physicochemical treatment. *Colloids and Surfaces C: Environmental Aspects* **2025**, *3*.

[10] Wu, L.; et al. Pilot-scale electrochemical advanced oxidation (EAOP) system for the treatment of Ni-EDTA-containing wastewater. *J. Hazard. Mater.* **2024**, *474*, 134840.

[11] Wu, Q. Y.; et al. Oxygen doping of cobalt-single-atom coordination enhances peroxymonosulfate activation and high-valent cobalt-oxo species formation. *Proc Natl Acad Sci U S A* **2023**, *120* (16), e2219923120.

[12] Wan, Z.; et al. Selective oxidation of emerging contaminants by high-valent cobalt(IV)-Oxo species: Constructing high-spin Co(III) sites in Fenton-like system. *Appl. Catal. B Environ. Energy* **2025**, *364*, 124852.

[13] Li, X.; et al. CoN_1O_2 single-atom catalyst for efficient peroxymonosulfate activation and selective Cobalt (IV)-O generation. *Angew. Chem., Int. Ed.* **2023**, *135* (27), e202303267.

[14] Li, X.; et al. Support work-function dependent Fenton-like catalytic activity of Co single atoms for selective cobalt(IV)=O generation. *Sci. Bull.* **2024**, *69* (24), 3867-3875.

[15] Wang, Y.; et al. Activation of peroxymonosulfate by sulfonated cobalt (II) phthalocyanine for the degradation of organic pollutants: The role of high-valent cobalt-oxo species. *Chem. Eng. J.* **2023**, *455*, 140671.

[16] Chen, F.; et al. Axial Co–O–Cu Pairs Enable Superexchange Interaction for Efficient Co^{IV}=O Formation toward Water Purification. *J. Am. Chem. Soc.* **2025**, *147* (46), 43086-43097.

[17] Su, R.; et al. Utilizing the oxygen-atom trapping effect of Co_3O_4 with oxygen vacancies to promote chlorite activation for water decontamination. *Proc. Natl. Acad. Sci. U.S.A.* **2024**, *121* (11), e2319427121.

[18] Su, R.; et al. Revealing the Generation of High-Valent Cobalt Species and Chlorine Dioxide in the Co_3O_4-Activated Chlorite Process: Insight into the Proton Enhancement Effect. *Environ. Sci. Technol.* **2023**, *57* (5), 1882-1893.

[19] Liu, B.; et al. Insights into the oxidation of organic contaminants by Co(II) activated peracetic acid: The overlooked role of high-valent cobalt-oxo species. *Water Res.* **2021**, *201*, 117313.

[20] Liu, B.; et al. Novel Nonradical Oxidation of Sulfonamide Antibiotics with Co(II)-Doped g-C_3N_4-Activated Peracetic Acid: Role of High-Valent Cobalt–Oxo Species. *Environ. Sci. Technol.* **2021**, *55* (18), 12640-12651.

[21] Rong, H.; et al. Electrochemical degradation of Ni-EDTA complexes in electroless plating wastewater using PbO_2-Bi electrodes. *Chem. Eng. J.* **2022**, *431*, 133230.

[22] Sun, Y.; et al. Electrochemical Ni-EDTA degradation and Ni removal from electroless plating wastewaters using an innovative Ni-doped PbO_2 anode: Optimization and mechanism. *J. Hazard. Mater.* **2022**, *424*, 127655.

[23] Zhang, F.; et al. Treatment of Ni-EDTA containing wastewater by electrochemical degradation using Ti^{3+} self-doped TiO_2 nanotube arrays anode. *Chemosphere* **2021**, *278*, 130465.

[24] Ye, X.; et al. Treatment of Ni-EDTA containing wastewater by electrocoagulation using iron scraps packed-bed anode. *Chemosphere* **2016**, *164*, 304-313.

[25] Qu, J.; et al. Ni-EDTA decomplexation and Ni removal from wastewater by electrooxidation coupled with electrocoagulation: Optimization, mechanism and biotoxicity assessment. *Sep. Purif. Technol.* **2025**, *376*, 133980.

[26] Huang, L.-Z.; et al. Ni(0) formation on carbon felt cathode triggers redox synergetic degradation of Ni-EDTA during electrochemical treatment for Ni-plating wastewater. *J. Hazard. Mater.* **2025**, *485*, 136851.

[27] Wang, M.; et al. Efficient removal of Ni-EDTA complexes utilizing 3D Ni-RM electro-fenton

system. *Sep. Purif. Technol.* **2025**, *369*, 133067.

[28] Zhao, Z.; et al. Enhanced removal of Ni-EDTA by three-dimensional electro-Fenton process using Fe-N-doped biochar as catalytic particle electrodes. *Chem. Eng. J.* **2023**, *471*, 144717.

[29] Xu, H.; et al. Minimizing toxic chlorinated byproducts during electrochemical oxidation of Ni-EDTA: Importance of active chlorine-triggered Fe(II) transition to Fe(IV). *Water Res.* **2022**, *219*, 118548.